Structure-Function Relationship of Iron Oxide Nanoflowers: Optimal Sizes for Magnetic Hyperthermia Depending on Alternating Magnetic Field Conditions

Megi Bejko, Yasmina Al Yaman, Auriane Bagur, Anthony C. Keyes Jr, Patrick Rosa, Marion Gayot, François Weill, Stéphane Mornet, Olivier Sandre

Optimal sizes of iron oxide nanoflowers for magnetic hyperthermia depend on the alternating magnetic field conditions

Megi Bejko[1,2], Yasmina Al Yaman[1], Anthony Keyes[1], Auriane Bagur[2], Patrick Rosa[2], Marion Gayot[3], Francois Weill[2], Stéphane Mornet[2]*, Olivier Sandre[1]*

[1] Univ. Bordeaux, CNRS, Bordeaux INP, LCPO, UMR 5629, 33600 Pessac, France

[2] Univ. Bordeaux, CNRS, Bordeaux INP, ICMCB, UMR 5026, 33600 Pessac, France

[3] Univ. Bordeaux, CNRS, PLACAMAT, UAR 3626, 33600 Pessac, France

* Correspondence: olivier.sandre@enscbp.fr (OS), stephane.mornet@icmcb.cnrs.fr (SM)

Abstract

Iron oxide nanoflowers can be synthesized through a polyol route firstly introduced almost 2 decades ago by Caruntu et al, presenting multi-core morphology, several grains (around 10 nm) being attached together (and obviously sintered). These IONFs present outstanding properties for magnetic field hyperthermia, which is considered as promising therapy against cancer. Although they have a significantly smaller diameter, the specific adsorption rate (SAR) of IONFs can reach values of the order of 1 $kW \cdot g^{-1}$, as large as for "magnetosomes" that are natural magnetic nanoparticles typically ~40 nm found in certain bacteria, which can be grown artificially but with lower yield compared to chemical synthesis. This work aims at better understanding the structure-property relationships between the internal nanostructure of IONFs as observed by HR-TEM and their properties, in particular magnetic ones. A library of mono and multicore IONFs is presented, with diameters ranging from 11 to 30 nm and narrow size dispersity. By relating their structural features (diameter, morphology, defects…) to their magnetic properties investigated in particular by AC magnetometry over a wide range of alternating magnetic field (AMF) conditions, the SAR values of all synthesized batches vary with overall diameter and number of constituting cores in qualitative agreement with theoretical predictions by the Linear Response Theory (LRT) at low fields or with the Stoner-Wohlfarth (SW) model for larger amplitudes, and with numerical simulations reported previously, in particular by showing a pronounced maximum at an IONF diameter of 22 nm.

Keywords: magnetic nanoparticles; polyol synthesis; multicore iron oxide nanoflowers; magnetic hyperthermia; specific absorption rate; AC magnetometry; dynamic hysteresis loops; HR-TEM; Fast Fourier Transformation (FFT); structural defects; disclination lines; planar inclusions; DC magnetization curves; specific magnetization; Field cooled and zero field cooled magnetization curves; effective magnetic anisotropy constant; Linear Response Theory (LRT); Stoner-Wohlfarth (SW) model.

1. Introduction

Iron oxide Nanoparticles (IONPs) have emerged in the last decades as an important tool that can lead to novel and useful avenues as nanomedicines to combat many medical conditions (cancers, infections...).[1,2,3] Their superparamagnetic properties have rendered these NPs useful in diagnostic as contrast agents for magnetic resonance imaging (MRI),[4] as well as in therapy as heat mediators for treatment of solid tumors by Magnetic Hyperthermia (MH) under an applied alternating magnetic field (AMF).[5] In addition, the magneto-thermal effect of IONPs has been exploited as an external stimulus to trigger drug release from drug-loaded magnetic thermosensitive nanocarriers, offering both temporal and spatial control.[6,7,8,9] Knowing these prospective applications that could lead to advanced diagnosis and treatment, a need for water-dispersible, nearly monodisperse, biocompatible IONPs with narrow size distribution and optimized magnetic properties is imperative.[2] Among the different types of IONPs, iron oxide nanoflowers (IONFs) synthesized through polyol route as firstly introduced by Caruntu *et al*.,[10] have gained attention due to their remarkable magnetic properties. These NPs are characterized by a multi-core structure as observed by TEM, presumably created through a mechanism of oriented aggregation of the nuclei formed by the iron oxide precursors,[11] while they appear as mono-crystals in HR-TEM, as if the nuclei were sintered altogether by the growth process, which is performed at reflux in a high boiling solvent (~220°C). This peculiarity is thought to be the cause of their high efficiency for magnetic hyperthermia,[12] which make them competitive even with the natural IONPs of largest diameter (~40 nm), denoted "magnetosomes".[13] Such structure of multiple cores linked together was shown to lead to a spin-glass state of the magnetic moments,[14] related to their high blocking temperature (T_B) as compared to mono-core IONPs of same diameter.

In the last decade, much effort has been devoted to synthesize IONFs with optimized heating efficiency *via* synthetic routes that can offer a better control on their size, shape and crystallinity, while being compatible with scale-up for further industrial development.[15] For this aim, the literature has shown many synthetic parameters worth investigating, including solvents of varying boiling temperatures (polyols, pure or mixed with poly(hydroxy) amines),[16] iron oxide precursors (chlorides, nitrates, acetylacetonate…),[17] concentration of added salts such as sodium acetate,[18] or polymers like poly(acrylic acid),[19,20] poly(ethylene glycol) (PEG)[21] or dicarboxy-PEG,[22] hydro- or solvothermal pressure (*i.e.* use of an autoclave),[23,24] or multi-step (seed-growth) method to prepare core-shell IONPs.[25] Instead of polyols, Spizzo *et al.* successfully used 2-pyrrolidone as other polar solvent of high boiling point for IONF synthesis,[26] whereas Zhang *et al.* used a polymer melt of 1000 g·mol^{-1} PEG as reaction medium, mixed with poly(vinyl pyrrolidone) (PVP) or poly(ethylene imine) (PEI)[18] as iron chelating polymers[27]. Nikitin *et al.* studied the thermal decomposition of $Fe(acac)_3$ complex in benzyl ether in presence of stoichiometric amount of 1,2-

hexadecanediol and of various organic acids, and also obtained IONF morphologies.[28] Finally, other authors reported the synthesis of multicore IONPs without the use of the polyol route, through an oxidative precipitation of iron(II) chloride in aqueous medium, in presence of carboxydextran as a chelating polymer,[29] or by an alkaline coprecipitation of $FeSO_4$ and $FeCl_3$ with multivalent alginate chains.[30] On our side, some of us showed in a previous work the utmost important role played by stoichiometric quantities of added water on the synthesis of IONFs, as ascribed to the forced hydrolysis mechanism.[31] In the same vein, Gavilán *et al.* compared these different synthetic methods for IONPs preparation in terms of simplicity, yield, quantity produced and also to obtain a general idea on how structural and magnetic properties are interrelated in these systems, which remains to this day a topic of great interest.[32,33] During the past decades indeed, many studies have shown the great impact of the size and size distribution as well as of the particle crystallinity and chemical composition, on the heating efficiency of the IONPs.[33,34,35] Theoretical predictions such as Linear Response Theory (LRT)[36] or the Stoner-Wohlfarth model[37] also demonstrated correlation between the field amplitude, the intrinsic properties of the NP and their heating power. Both models predict a sharp maximum of the heating power for a well-defined diameter at certain field conditions followed by an abrupt decrease when the mean particle size differs only by a few nanometers with respect to the ideal size.[38] This size optimum has been observed experimentally for iron oxide or pristine iron NPs with a nearly-spherical,[39,40,41] or a cubic morphology.[42,43] Concerning truly multicore IONFs or simply clustered IONPs (*i.e.* without being monocrystalline),[12] the magnetic behavior appears in all cases to be governed by intra-particle characteristics *i.e*. intra-particle dipolar interactions and surface spin disorder (aka spin-canting) which both play on the magnetic anisotropy energy, the impact of which is illustrated in several studies. For instance, Blanco-Andujar *et al.* reported that magnetic interactions alongside with the number, size and spatial arrangement of the cores directly affect the final heating properties of IONFs obtained by a microwave synthesis in the presence of citrate ligands.[44] Similarly, Storozhuk *et al.* reported an exceptional enhancing of the heating power of IONPs when increasing their size *via* a seeded-growth strategy. However, previous study by Lévy *et al.* had shown that simple IONP size growth without reaching monocrystalline state is not sufficient to raise the heating properties.[38] The positive impact of the size increase on the heating rate necessitates that the enhanced magnetic exchange couplings within the cores overrides the negative effect of structural defects and misalignments that inevitably arise between the cores during the seeded growth step of the IONPs.[45] On the other hand, defects can also be beneficial to increase the magnetic anisotropy energy (originating from shape or surface), eventually improving the heating properties,[46] which explains the higher SAR observed for magnetic nanocubes as compared to nanospheres of same volume.[42] In all cases the balance between inter-core magnetic dipolar interactions *versus* exchange energy between magnetic domains can induce the appearance of a size optimum exhibiting exceptional heating properties, as reported for 50 nm iron oxide nanoclusters exhibiting “superferrimagnetic” behavior.[19]

More recently, Bertuit *et al.* implemented the polyol synthesis route of IONFs in continuous flow by controlling the heating ramp to 220°C between 2°C·min^{-1} and 8°C·min^{-1}, with a residential time in the millifluidic reactor between 1 and 2 h. They reported linear dependence between the SAR of IONFs with their mean number of cores (N_{core}), as estimated by the ratio of the physical volume (determined by TEM) divided by the volume of the magnetic domains (assessed by fitting the magnetization curve with Langevin's function). The linear dependence of the heating rate with the number of grains was interpreted by the exchange energy couplings between the cores, estimated proportional to N_{core} (assuming the average number of neighbors around a given core in a cluster is constant).[47] Nevertheless, in all the studies aforementioned, the evaluation of the heating power and its dependence with structural parameters, is generally done under limited AMF conditions of amplitude and frequency. Subsequently, this restricts our understanding of how the magnetic field conditions alongside with the intrinsic properties of the IONPs itself can affect their heating efficiency. With this in mind, we propose in this paper to full investigate the structure-properties relationship existing between all the parameters known to influence the magnetic properties of IONPs: size, morphology, structural defects, and composition, as well as the characteristics of the applied AMF. For this purpose, the heat efficiency was measured under a wide range of AMF conditions and for a library of IONPs and IONFs prepared by slightly changing the classic polyol conditions originally published by Caruntu *et al*.[10] More precisely, adding H_2O and modifying the solvent ratio or the cooling temperature ramp enabled to create a whole library of monocore IONPs and multicore IONFs with narrow mean size variation between the synthesized batches (less than 5 nm), with diameters ranging from 11 to 30 nm. The selected size range was intentional, since it corresponds to sizes of interest for biomedical applications as well as to the upper and lower limits of validity of respectively LRT and Stoner-Wohlfarth theories.[48,49] In-depth multiscale characterization of the synthesized NFs was carried on, starting from their structural features (overall diameter, morphology *i.e.* mono or multicore, number and size of cores, crystal size and defects) and chemical composition to their magnetic properties probed under static magnetic field (saturation magnetization, blocking temperature, anisotropy energy constant, and magnetic domain size). Lastly, the heating performances of the IONPs were investigated by AC magnetometry where the specific adsorption rate (SAR, expressed in W·g^{-1} of γ-Fe_2O_3) is determined on a wide range of field conditions from the direct integration of the hysteresis loop surface area of the dynamic magnetization curves $M(t)$ *vs.* $H(t)$ measured using so-called pick-up coil instrument.[50,51,52] The commercial set-up employed allows working under a wide range of magnetic field amplitude H varying from 4 to 24 kA·m^{-1} with increments of 4 kA·m^{-1} and for frequencies in the range of 146-344 kHz.[53] This way, the variation of the SAR of all the synthesized batches with overall diameter (from TEM) as well as crystal size (from XRD) and magnetic domain size (from the fit of VSM curves) was evaluated under 24 different AMF conditions within reasonable experimental time. By gathering the results obtained from structural and magnetic analyses of the

IONPs and of their heating power determined under a wide range of AMF conditions (amplitude and frequency), we were able to draw a complete picture on how all these parameters are interrelated within these systems. The results shown in this manuscript demonstrate how the heating efficiency of IONFs obeys complex interdependent manner, varying not only with the size, structure and morphology of the NFs but also with the selected AMF conditions, following the predictions of either Stoner-Wohlfarth or LRT theoretical models and joining the previously reported numerical simulations of Mehdaoui *et al.*[40] but also of Engelmann *et al.*[54,55] for the variation of SAR with sizes under various AMF conditions. Furthermore, the limits in terms of reproducibility and yield of the polyol route for producing performant IONFs as heat mediators for MH is also discussed in this report, stressing the need to find optimized and scaled-up conditions to translate the polyol method into robust industrial production of IONPs that are the most efficient for biomedical applications.

2. Materials and Methods

2.1 Materials

Iron (II) chloride tetrahydrate ($FeCl_2 \cdot 4H_2O$, 98%), iron (III) chloride hexahydrate ($FeCl_3 \cdot 6H_2O$, >97%), iron (III) nitrate nonahydrate ($Fe(NO_3)_3 \cdot 9H_2O$, >98%), diethylene glycol (DEG, 99%), *N*-methyldiethanolamine (NMDEA, 99%), sodium hydroxide micro-pellets (NaOH, 98%), fuming nitric acid (HNO_3, 69%), ethanol (EtOH), acetone, and ethyl acetate (EtAc) were purchased from Thermo Fisher Scientific (Karlsruhe, Germany) or Sigma-Aldrich (St Quentin Fallavier, France) and used without further purification.

2.2 Synthesis, oxidation and isolation of IONPs

The original protocol by Caruntu *et al*.[10] was reproduced, with some adjustments, in particular the addition of a controlled amount of deionized water in the medium.[31]

2.2.1 Synthesis of nanoflower batches named NF3, NF4 and NF5 through classic polyol route conditions

A mass of 1.082 g (4 mmol) of $FeCl_3 \cdot 6H_2O$ and 0.398 g (2 mmol) of $FeCl_2 \cdot 4H_2O$ is dissolved in 80 g of a liquid mixture of DEG and NMDEA with 1:1 (v/v) ratios (solution A). The resulting solution was then flushed with inert gas (N_2 or Ar) under stirring for 1 h. In parallel, 0.64 g (16 mmol) of NaOH was dissolved in 40 g solution of polyol 1:1 (v/v) in an ultrasound bath and flushed with inert gas under stirring for 1h (solution B). Then, solution B was added to the solution A in a tricol flask of 250 mL and the resulting mixture was flushed with nitrogen or argon for 15 min and proceeded to heating with a ramp of $2°C \cdot min^{-1}$ up to 220°C using an electronically controlled Digi-Mantle™ dry heater (Electrothermal™ OMCA0250) under mechanical stirring at 400 RPM with a Teflon stirring rod. After 4 h of

reaction at reflux, the resulting black suspension of magnetite Fe_3O_4 NPs in the tricol flask was removed from the heating mantle to proceed with washing and oxidation.

2.2.2 Synthesis of NF1

For the synthesis of this batch, the quantities of $FeCl_3 \cdot 6H_2O$, $FeCl_2 \cdot 4H_2O$, NaOH and the volume ratios of DEG and NMDEA solvents for the production of solution A and B were identical to the classic polyol protocol as described in 2.1.1. However, after adding solution B to A and stirring for 10 min under inert gas, 5.5 mmol (100 µL) of H_2O was added to the mixture at room temperature, followed by stirring and flushing for 10 min with inert gas. The following was identical to the classical protocol: the mixture was heated with a ramp of $2°\cdot min^{-1}$ up to 220°C under mechanical stirring at 400 RPM with a Teflon stirring rod. After 4h of reaction at reflux, the resulting black suspension of magnetite Fe_3O_4 NPs was removed from the heating mantle to proceed with washing and oxidation.

2.2.3 Synthesis of NF2

For the preparation of the solution A, the same quantities of iron salts as indicated in 2.1.1. were added in 80 g liquid mixture of DEG/NMDEA with volume ratios of 1.5:1 (instead of 1:1) and stirred under inert gas for 1h. In parallel, for the preparation of solution B, the NaOH pellets were added to 40 g liquid mixture of DEG/NMDEA with volume ratios of 1.5:1 and stirred under inert gas for 1h. Then, solution B was added to the solution A and the resulting mixture was flushed with inert gas for 15 min and heated with a ramp of $2°C\cdot min^{-1}$ up to 220°C under mechanical stirring at 400 RPM with a Teflon stirring rod. After 4h of reaction at reflux, the resulting black suspension of magnetite Fe_3O_4 NPs was removed from the heating mantle to proceed with washing and oxidation.

2.2.4 Synthesis of NF6 and NF7

For the synthesis of NF6 and 7, the synthetic procedure as well as the quantities of $FeCl_3 \cdot 6H_2O$, $FeCl_2 \cdot 4H_2O$, NaOH and the volume ratios of DEG and NMDEA solvents for the production of solution A and B were identical to the classical polyol protocol as described in 2.1.1. After adding solution B to A, the resulting mixture was flushed with argon for 15 min and heated with a ramp of $2°C\cdot min^{-1}$ up to 220°C under mechanical stirring at 400 RPM with a Teflon stirring rod. After 4h of reaction at reflux, the heating was turned off and the resulting black suspension of magnetite Fe_3O_4 NPs was left cool down slowly overnight to room temperature under inert gas flushing on the hot heating mantle. The washings and oxidation steps were done the morning after, in this case.

2.2.5 Washing and isolation

After cooling down to room temperature (either slowly or rapidly), the suspension was poured into a 500 mL beaker and settled on large ferrite magnets ($152\times101\times25.4$ mm^3, Calamit Magneti™, Milano-Barcelona-Paris) for

10 min. After removing all the polyol supernatant by aspiration, a large volume of 1:1 mixture (v/v) of EtAc and EtOH was used to wash the solid, which was re-suspended by mechanical stirring for 15 min at 200-250 RPM. After magnetic settlement, the supernatant was again aspirated, and the nanoparticles were transferred into a smaller beaker (50 mL). The washing procedure with EtAc/EtOH mixture was repeated 3 times to remove any organic layer covering the nanoparticles originating from polyol decomposition.

2.2.6 Acidification and oxidation to γ-Fe_2O_3

Next, following method introduced by Tourinho *et al*.,[56] 8.25 g of iron (III) nitrate was dissolved in 20 mL of water and boiled before adding to the pellet of nanoparticles. The resulting suspension was heated to 80°C for 45 min (maximum duration) to achieve complete oxidation of the nanoparticles (color shifts from black to brown). The suspension was decanted on the permanent magnets to isolate the nanoparticles from the solution. Once aspirated, another 40 mL of a 10 wt % HNO_3 (2 M) solution was added, and the resulting suspension was stirred for 10 min. After magnetic sedimentation, the supernatant was aspirated and then replaced by acetone. After stirring for 5 min, the suspension was magnetically decanted, and the supernatant was aspirated. The same washing steps were repeated once with acetone and twice with diethyl ether. A final aspiration was done and then 20-30 mL of deionized water was added to the nanoparticles, which readily disperse. The colloidal suspension was then sonicated for 10 min (Sonics 130 W Vibracell™) to break possibly remaining aggregates and fully disperse the nanoparticles as a stable ferrofluid with final pH~2 (dilute HNO_3), which should be maintained near this value to keep colloidal stability during any further dilution for the study of the IONP properties.

2.3 Characterizations of the IONPs

2.3.1 Determination of γ-Fe_2O_3 concentration

This solid weight concentration in iron oxide was assessed by a photometric method after mineralization of the IONPs, using the characteristic absorption peak at 350 nm of $[Fe(Cl)_6]^{3-}$ complex when an aliquot of the suspension was completely dissolved in concentrated hydrochloric acid (HCl 5 M), according to a previously determined calibration line.[57]

2.3.2 Visible-Near Infrared (NIR) spectra of IONPs

The absorbance spectra of IONPs were recorded on a Shimadzu 1800 Double Beam UV-Vis Spectrophotometer. For this, the concentration of the NPs was set at 0.32 $g \cdot L^{-1}$ (2 mM γ-Fe_2O_3 *i.e.* 4 mM Fe^{3+}) by dilution in HNO_3 10 mM (pH~2). Then, 3 mL of the dispersion was put into a quartz cell (light path *L*=1 cm). The spectra were then recorded from 400 to 1100 nm, using pure solvent (dilute HNO_3 at pH~2) in the reference beam.

2.3.3. Luminescence spectra of IONFs

Luminescence emission spectra was recorded on a Jasco Spectrophotometer FP-8500. The NPs were previously diluted at 0.32 $g{\cdot}L^{-1}$ (2 mM γ-Fe_2O_3 *i.e.* 4 mM Fe^{3+}) in HNO_3 10 mM and transferred in a quartz cuvette (*L*=1 cm). The excitation wavelength was set at 232 nm with a scan speed of 100 $nm{\cdot}min^{-1}$ and with bandwidths of 20 nm for both excitation and emission.

2.3.4 Transmission electron microscopy

Direct observation of the size, size distribution and morphology of the nanoparticles were made by transmission electron microscopy (TEM), on a Jeol JEM-1400+ instrument operated at 120 kV and digital micrographs were obtained with a Smart Orius 1000 Gatan camera. High resolution images were obtained with a Jeol 2200FS microscope equipped with a 2k pixel Gatan Camera while selected area electron diffraction patterns (SAED) were made on a Jeol 2100 microscope equipped with an Orius 200D Gatan camera. All these microscopes are available at PLACAMAT platform, Bordeaux.

Prior to the observation, the colloids (10 µL, 0.2 $g{\cdot}L^{-1}$ γ-Fe_2O_3) were deposited onto TEM copper grids (lacey/thin double carbon film Cu-300LD, 300 mesh, Pacific Grid Tech, San Francisco, CA). The excess of the droplet was aspirated with a filter to leave a thin liquid film onto the TEM grid. The grids were then left to dry for 10-15 min before the analysis.

NP size distribution and diameter was obtained by measuring the diameters of ~300 NPs of each batch with ImageJ software (https://imagej.nih.gov/ij/). Size-histograms were fitted to a normal distribution law via Origin software. The morphology proportion of spherical (monocore) NPs and flower NPs (multicore) was determined by counting the number of each type of NP on the TEM images. For each batch, a total number of NPs *N*>300 was considered to determine the morphological statistics. The constituting core diameter of the multicore NPs was determined by measuring the average size of the cores on both high magnification (> 60000×) and HR-TEM images using ImageJ software. For a better estimation of the core size, the measurement was done on numbers of cores *N*~250 for NF3, NF4, NF5, NF6, and NF7 batches and on *N*~120 for NF2.

2.3.5 X-ray powder diffraction

X-ray powder diffraction (XRPD) was realized on a PANalytical X'pert Pro diffractometer equipped with Cu radiation. The samples were dried and the powder evenly spread onto a Si wafer for the analysis. Patterns were analyzed with the HighScore and Eva softwares to obtain the crystallographic unit cell as well as the crystal size from the Debye-Scherrer equation.

2.3.6 Dynamic light scattering

Dynamic light scattering (DLS) operated in backscattering mode *i.e.* at 165° angle (Vasco™ Flex, Cordouan Technologies™, Pessac, France) was used to calculate the hydrodynamic intensity-average size and polydispersity index (PDI) defined as the ratio of the 2nd order coefficient to the square of the 1st order coefficient in the Cumulant series analysis of the autocorrelation curves, as well as multimode Padé-Laplace algorithm.[58] In practice, five runs of 40 s duration were acquired, the *Z*-average diameter (Z_{ave}) and PDI were averaged and a standard deviation was calculated from the statistics of the five runs. Besides, the broadness of the size distribution was estimated using $Z_{ave} \times PDI^{0.5}$ according to standard method of light scattering data analysis.[59]

2.3.7 Magnetic heating efficiency measured by AC magnetometry

Dynamic hysteresis loops were measured by AC magnetometry with a pick-up coil technology[50] using the AC Hyster™ setup commercialized by NanoTech Solutions company (Ntsol, Madrid, Spain). An aliquot of 40 µL suspension in the concentration range 4-12 $g \cdot L^{-1}$ (containing a dry γ-Fe_2O_3 mass typically ≈ 1-5 $\times$ 10^{-7} kg) was put at the bottom of a 3 mm diameter 4 inches length NMR tube (VWR, France). Then the magnetization cycles *M*(*H*) were measured thrice (waiting 45 s between each measurement for the sample to cool down) at a series of magnetic field amplitudes (H_{max}) ranging from 4 to 24 $kA \cdot m^{-1}$ and at frequency (*f*) varied in this series: 146, 217, 280 and 344 kHz. The three measured cycles were averaged and normalized by the exact weight of iron oxide known from iron titration to compute the mass magnetization in $A \cdot m^2 \cdot kg^{-1}$. To cope with unavoidable drifts of the pick-up coil calibration, each curve *M*(*H*) was adjusted by a normalization factor so that the mass magnetization measured under an AMF of amplitude H_{max}=24 $kA \cdot m^{-1}$ was identical to the value measured by VSM magnetometry under a DC magnetic field of same intensity H_{DC}=24 $kA \cdot m^{-1}$. The validity of the SAR measurement by AC magnetometry was double-checked for some samples by determining it also by the classical yet much more time-demanding calorimetry method in the same AMF conditions, showing good agreement between the two methods as previously shown in literature.[51,53]

2.3.8 Static magnetization curves *versus* field

Magnetization experiments under DC field were conducted on a Vibrating Sample Magnetometer (VSM) Microsense EZ-7. For this measurement, the samples were diluted at 2 $g \cdot L^{-1}$ γ-Fe_2O_3 in HNO_3 10 mM (pH~2) and an aliquot of 20 µL was added in Ag sample holders. The magnetization was then recorded under a range of applied magnetic field intensities *H* from 0 to 1430 $kA \cdot m^{-1}$ (B_{max}=1.8 T) with regularly spaced data points and at least 40 measurements in the low-field region (*H*<475 $kA \cdot m^{-1}$ or *B*<0.6 T).

2.3.9 Magnetization curves *versus* temperature

Zero Field Cooled (ZFC) and Field Cooled (FC) (ZFC/FC) magnetization curves were measured on a VSM Microsense EZ-7 under a wide temperature range (100-420K). For this, 100 µL of NPs diluted in HNO_3 10 mM (pH~2) to 0.1 $g \cdot L^{-1}$ γ-Fe_2O_3 were added in rectangular cotton pieces of 0.072 cm^3 (0.6×1.2×0.1 cm) and then dried at 70°C for 3 h. For the ZFC measurement, the dried cotton pieces were firstly cooled down to T=100 K under zero applied magnetic field. Then the sample was exposed to a low applied magnetic field H_{DC}=4 $kA \cdot m^{-1}$ during the heating from 100 to 420 K. For the recording of the FC curve, the cooling down of the sample was performed while applying the same magnetic field H_{DC}=4 $kA \cdot m^{-1}$.

3. Results

3.1. Structural analysis of IONPs

3.1.1. Size and morphology of IONPs

The synthesis of the IONPs studied in this manuscript was inspired by the polyol route originally published by Caruntu *et al.*[10] As described in Materials and Methods section 2.2.1, the classic polyol conditions for IONPs synthesis were repeated 3 times in order to check their repeatability by producing batches named NF3, 4 and 5 shown in **Figure 1(c-e)**. The physical diameter (d_{TEM}) of the NPs determined through TEM image analysis of N=300 NPs are gathered in **Table 1** and their corresponding size histograms in **Figure S1** of Supporting Information (SI). The TEM images show the presence of flower morphology made by the aggregation of small cores into multicore NPs or "nanoflowers" (NF) as well as spherical *i.e.* monocore NPs. A morphological study on N≈350 NPs was performed on the TEM images in order to determine the proportions of respectively multi and monocore NPs. In all cases, as shown in the pie-charts of **Figure 1(c-e)**, the majority of produced IONPs under classical polyol conditions exhibit multicore morphology (>60%), accompanied by low size dispersity as well as narrow size variation between the batches (d_{TEM} ranging from 20.9 (NF3) to 23.2 nm (NF5), less than 2 nm variation). In order to decrease the size of IONPs, two strategies involving the synthetic conditions of the polyol route were considered: 1/ Prior addition of H_2O in the polyol mixture based on the previous work of Hemery *et al.*[31] and 2/ Increase of DEG content. For the 1st strategy, 100 µL of H_2O representing only 0.083% of the total volume was added prior to heating as described in Section 2.2.2. The slight water content in the polyol medium not only plays an important role in decreasing the size of the NPs down to 11.8 nm but also significantly decreases the ratio of multicore NPs down to 8% when compared to the classic protocol. Thus, almost all the NPs are monocore with a spherical morphology as represented on **Figure 1(a)**. This incorporation of a stoichiometric amount of water in the highly hygroscopic polyol solvent mixture has a positive effect on the "forced hydrolysis" mechanism by inducing faster nucleation of more numerous nuclei, which in turn produce smaller, spherical NPs.[31] The 2nd

strategy consists in increasing the DEG content in the polyol composition without changing the concentration of NaOH and iron salts. The change of solvent ratio from 1:1 to 1.5:1 DEG/NMDEA induced a slight decrease in the diameter (batch NF2 **Figure 1(b)** of d_{TEM}=16.4 nm) when compared to the original polyol conditions followed by a change in the morphology of the NPs. Similar to the H_2O adding, increasing the amount of DEG reduced the multicore proportion of the NPs down to 27% when compared to the classic polyol conditions, with the dominant morphology being spherical monocore NPs (70%). This result was predictable, since reducing the amount of NMDEA, a stronger chelator than DEG for the surface of iron oxide and necessary for flower morphology, modifies the interactions between the nuclei. As reported by several works, IONF synthesis departs from classical nucleation and growth mechanism by comprising an orientated aggregation step.[32,60] In the limit where the synthesis is conducted in pure DEG, it is known to produce ultra-small iron oxide nanospheres, especially under very efficient heating in a microwave oven.[61] Bertuit *et al.* reported similar results to us, where mixed morphologies of flower and spherical 14 nm IONPs were obtained by the use of a fast heating ramp (8°C·min^{-1}) instead.[47] We note that besides the heating ramp, the change of solvent ratio as well as the adding of H_2O produce the same effects due to a faster nucleation step, *i.e.* size decrease and change in morphology of the NPs. On the other hand, producing IONPs with larger diameters than the classical route is possible by increasing the heating duration of the polyol solvents. Thus by playing on the growth and ageing times of the NPs, differences in the size of IONPs were observed when compared to the classic polyol conditions. IONPs possessing larger diameters (batches NF6 and 7 with TEM diameters of 28.7 nm and 29.3 nm, respectively **Figure 1(f-g)**) were synthesized by letting the NPs cool down slowly overnight on the heating mantle under the hood while flushing inert gas, instead of fast cooling to RT. The diameter increase is then ascribed to extended reaction time by which the IONPs can continue to grow by Ostwald ripening or by coalescence.[62] Additionally, almost all the produced NPs (up to 85%) in NF6 and NF7 were multi-cores. This corresponds to 25% increase of multicore proportion compared to the classic polyol route. When comparing how morphology yields evolve with the mean size of the NPs, a trend towards higher proportions of well-defined multicore NPs is seen when increasing their size as shown in **Figure 1 (h)**, directly linked to the differences between the nucleation, growth and ageing steps induced by changing the synthesis parameters. Our results joins the report of Bertuit *et al.*[47] showing that slower nucleation favors the synthesis of multicore NPs whereas fast nucleation produces spherical monocore NPs. Furthermore, the fine structural analysis by electron tomography presented on the report of Lartigue *et al.*[63] showed that the nanoflowers synthesized through polyol route are isotropic assemblies of merged cores, forming nearly spherical "supercrystals" with the overall diameter depending directly on the number of cores.

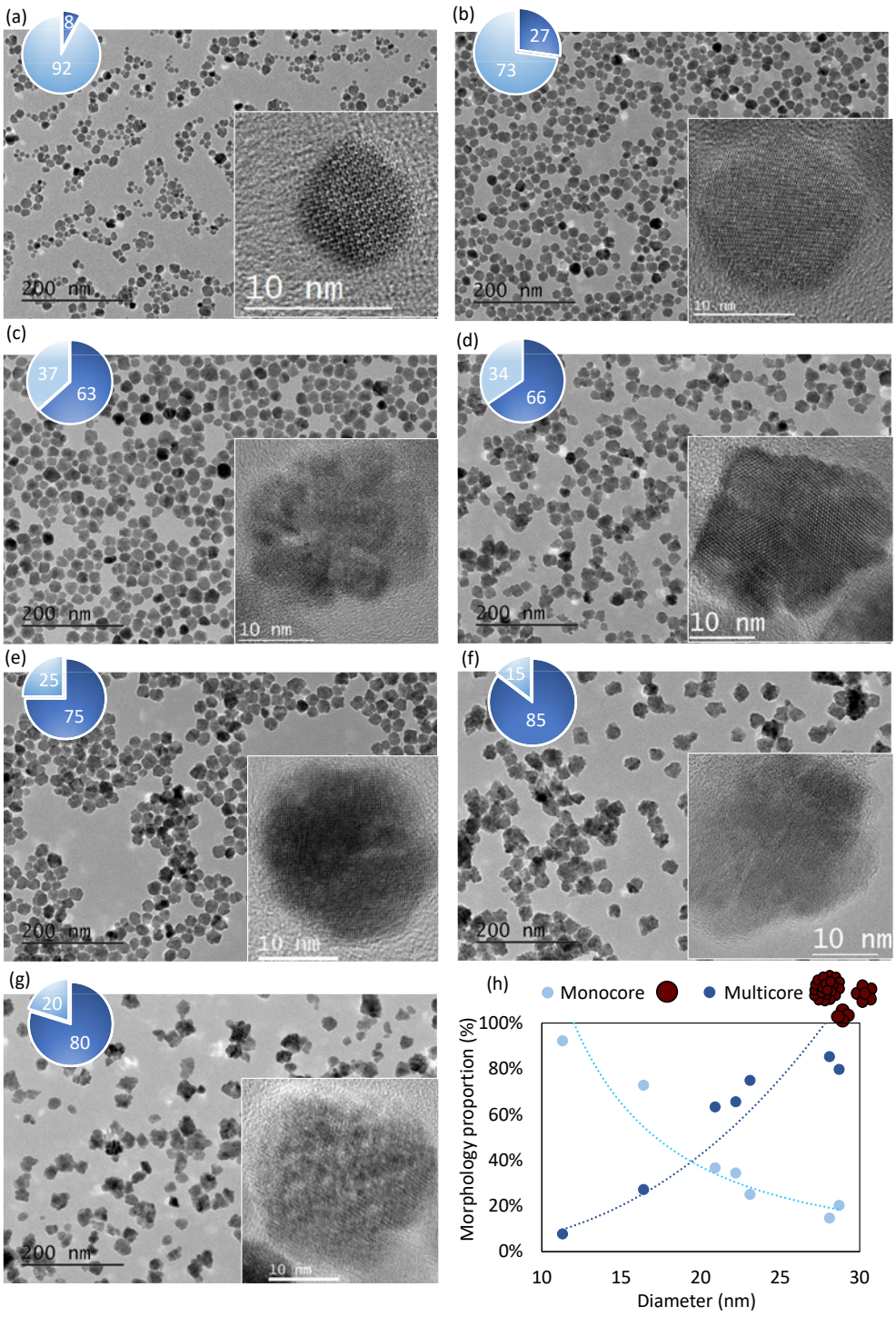

Figure 1. TEM micrographs of IONPs synthesized with (a) H_2O adding (NF1), (b) DEG content increase (NF2), (c-e) classical polyol conditions (NF3-5 respectively) and (f-g) extended reaction time (NF6-7). The pie charts show the proportion of the batches in multicore NPs (dark blue) and monocore NPs (light blue). The insets show high-resolution micrographs of the

IONPs. (h) Evolution of the NPs morphology with d_{TEM}. The corresponding size-histograms are gathered in **Figure S1** in Supplementary Information (SI).

This allows us to estimate from TEM images not only the overall diameter of the NPs (d_{TEM}), but also the diameter of the individual cores composing the nanoflowers, d_{core}. Thus, the latter was evaluated by manual counting on TEM images of N≈250 NPs for batches NF3-7 and of N=150 NPs for NF4, due to its lower proportion in flowerlike NPs (27%, **Figure 1(b)**). By this way, an estimate of the number of cores was determined from the ratio:

$$N_{core}=(d_{TEM}/d_{core})^3 \qquad \text{Eq. (1)}$$

Please note that for better approximation of the mean core number on the polymorphous samples, the spherical proportion was taken in account by considering its core number as $N_{\mathrm{core}}^{\mathrm{S}}$=1. For instance, the NF6 batch with 85% of flowerlike multicore NPs with $N_{\mathrm{core}}^{\mathrm{F}}$=34.8 and 15% of spherical NPs with $N_{\mathrm{core}}^{\mathrm{S}}$=1 gives finally $<N_{core}>$=85%×34.8+15%×1=29.7. From the values of d_{core} and N_{core} gathered in **Table 1**, one can notice that all the samples exhibit similar d_{core} values (apart from NF7). This leads to an increase of $<N_{core}>$ with the external diameter of the NPs varying roughly with the third power of d_{TEM} (**Figure S2** of Supporting Information SI) as the nanoflowers appear to be sintered as close-packed clusters of nuclei which have more or less the same unit core size ~10 nm

3.1.2. Dispersion state of the IONPs

The dispersion state of the different IONPs batches was assessed by dynamic light scattering (DLS) in a weakly acidic aqueous medium (10 mM HNO_3 pH~2). Due to the multimodal nature of our batches related to their size distribution and morphology, the hydrodynamic diameters D_H were estimated both from the Cumulant analysis, yielding the Z-average (D_Z) and PDI, and from the Padé-Laplace algorithm, which values are all gathered in **Table 1**. Padé-Laplace algorithm, more adapted for multimodal NP distribution, indicates presence of two populations (D_1 and D_2): a main class of NPs with hydrodynamic sizes D_1 in accordance with d_{TEM} for all batches, and a second population of larger NPs, smaller in number yet highly contributing to the scattered light intensity in DLS. The Z-average values are found in between D_1 and D_2, and range from 30 nm (NF1) to 82 nm (NF7). PDI values higher than 0.20 indicate sample polydispersity, related to their broader size distribution as well as mixture of morphologies or slight aggregated state, as evidenced by TEM. Interestingly, sample NF1 has the largest PDI, even when compared to sample NF7, the latter having the largest size distribution as evaluated by TEM (**Figure S1 (g)**). This indicates that the high polydispersity of NF1 is a direct consequence of the presence of several size populations as shown in **Figure 1(a)** as well as the presence of a low proportion of aggregates scattering light much more than smaller NPs (from the Rayleigh law of scattering in the sixth power of particle radius) and thus

contributing way more to the D_Z intensity-weighting. In addition, the large D_Z recorded for NF6 and NF7 is ascribed to presence of a small proportion of very large NPs, as evidenced by D_2 in the Padé-Laplace calculation.

3.1.3. Crystal structure and composition of the IONPs

To get better insight on the crystal structure of studied samples, SAED as well as powder XRD characterization were performed on all of them. Detailed SAED patterns of the sample library are shown on **Figure S3**. For all the samples, the observed reflections are consistent with cubic lattice with a lattice parameter around 8.37 Å and a Bravais lattice F. Note that the intrinsic precision of the determination of the lattice parameters by electron diffraction does not allow to detect any difference of the crystallographic parameter from one sample to another one. Similar to SAED, the XRD patterns (**Figure S4 (a)**) are identical for all sets of NFs. The reflections match with the expected Bragg peaks of magnetite Fe_3O_4. Both of these diffraction techniques do not permit the validation of the oxidation step of IONPs since depending of the oxygen vacancy ordering, maghemite and magnetite can crystallize in the same space group. However, the XRD patterns give us information on the lattice parameter as well as the crystal size of IONPs. The lattice parameter *a* was retrieved from XRD data refinement, the values of *a* for each NP are gathered in **Table 1**. The cell parameters of all samples lie in between the values of bulk maghemite (8.346 Å, JPCDS 39-1346) and bulk magnetite (8.396 Å, JCPDS 19-0629), indicating that the oxidation step is incomplete, leaving magnetite rich zones within the samples. Furthermore, many reports have shown that the oxidation step of IONPs is a size-dependent process, with maghemite being the dominant phase of small-sized NPs when compared to larger ones.[64,65] An easy way to assess the oxidation state of NPs and its evolution with size consists in monitoring the near-IR optical (NIR) band above 1000 nm assigned to intervalence charge transfer (IVCT) between Fe^{2+} and Fe^{3+} in magnetite only.[66] The loss of the NIR band of magnetite indicates its oxidation into maghemite. The visible-NIR absorbance spectra was recorded for IONPs NF1, 2, 3, 5 and 6 with sizes (d_{TEM}) 11.8, 16.4, 20.9, 23.1 and 28.7 nm respectively, to check the evolution of magnetite content with size. As shown by the absorption spectra in **Figure S4 (b)**, the lowest optical absorbance in the NIR region was recorded for the smallest sample NF1, indicating the highest content of maghemite amongst the series, as expected. On the other hand, the optical absorbance in the NIR increases progressively with size. Samples NF2 (16.4 nm), NF3 (20.9 nm), NF5 (23.1 nm) and NF6 (28.7 nm) exhibit higher molar extinction coefficients in the NIR (defined relatively to atomic Fe content), indicating higher content in magnetite when compared to NF1.

From the XRD data, monocrystal size of the IONPs was deduced from the peak broadening effect by applying the Scherrer equation on the most intense peaks of the XRD diffractogram:

$$\tau = \frac{k\lambda}{\beta \cos(\theta)} \qquad \text{Eq. (2)}$$

where k is the form factor (0.89 for spherical NPs), λ the X-ray wavelength, β the peak full width at half maximum (FWHM) intensity, and θ the Bragg diffraction angle.

With this formula, crystal sizes (d_{XRD}) of 10.4 and 16.9 nm were estimated for NF1 and NF2 respectively, values quite close to their TEM core sizes (~11.8 and 16.4 nm), suggesting that these batches, mainly composed of spherical NPs, are monocrystalline. Similarly, for the larger IONPs possessing high proportions of multicore NPs (from NF3 to 7), the crystal size is almost always close to the TEM outer diameter d_{TEM}. This indicates that the small cores presumably have gone through an epitaxial growth and share the same crystal orientation, a growth mode called "oriented aggregation" firstly reported for iron oxyhydroxide nanocrystals.[11] HR-TEM images showed in **Figure 1** confirm the results obtained by XRD where for each sample, continuous crystallinity throughout the volume of the flower was observed.

Inverse Fourier transform analysis of the HR-TEM images enables to distinguish crystalline defects present on different crystal planes for all the set of IONPs. **Figure 2** compares the (220) crystal plane of samples: NF1 and 2 composed mainly by monocore NPs and NF4 and 6 by multicore NPs. The inverse Fast Fourier transformation (iFFT) images of NF1 and NF2 present no defects within the crystal plane (220) as shown in **Figure 2 (c)** and **(f)**. On the other hand, the iFFT of NF4 and 6 (**Figure 2 (i)** and **(l)**), which correspond to samples of predominantly possessing a multicore morphology and $<N_{core}>$, demonstrate the presence of misalignments in the (220) plane. In addition, the structural defects predominantly present on multicore NPs are situated near the surface borders (as shown for NF3 and 4 in **Figure S5 (c)** and **(f)**) or within the structure, near the borders of the constituting cores (as shown in **Figure S5 (i)** for NF6). However, since beam-related artefacts may occur during HR-TEM analysis, the presence of structural defects was evidenced through fluorescence spectroscopy as well, by recording the NP emission after UV excitation at 232 nm. For all set of NPs, a main peak centered at ~560 nm was observed as shown in **Figure S6 (a)** and **(b)**, which has been ascribed to the presence of interstitial oxygen atom defects.[47,67,68,69] Based on the report of Sadat *et al.*, the observed photoluminescence (PL) is due to radiative recombination of mobile electrons from e_g to t_{2g} on octahedral sites of iron oxide.[70] Bertuit *et al.* has recently reported that the PL intensity of IONPs is highly enhanced with the concentration of emitting defects.[47] In our case, the maximum PL intensity increases linearly with $<N_{core}>$ as shown in **Figure S6 (c)**. Interestingly, when normalized with the $<N_{core}>$ concentration, the maximum PL intensity increases with d_{TEM} following a power law of exponent nearly 2 (illustrated in **Figure S6 (d)**). This indicates that the PL intensity as well as emitting defect concentration varies as the area of the NF outer surface, in good correlation with the defect study by HR-TEM showing misalignments near the NF surface, with larger NPs of higher $<N_{core}>$ possessing higher defect occurrence than monocore NPs. It is worth noticing that NF6, which has the largest diameter as well as $<N_{core}>$ number, has also the highest PL

intensity when compared to all other samples. Furthermore, NF4 (22.2 nm) exhibits also higher PL intensity indicating higher defect density when compared to analogous batches NF3 (20.9 nm) and NF4 (23.4 nm).

Higher occurrence of defects in multicore NPs gives also insights on their nucleation and growth mechanisms. For multicore NPs, once small nuclei form in the polyol medium, they tend to aggregate to minimize their high surface energy. Then these small cores in close contact rotate relatively to each other such as sharing the same crystal orientation than their neighbors. This so called "oriented aggregation" process creates multicore NPs, yet giving rise to small crystal defects in between the cores forming the NP. However, these topologic defects (such as disinclination lines or planar inclusions) are insufficient to create real grain boundaries, as all the cores share same crystallographic orientation of their atomic planes. On the other hand, spherical NPs follow a more classical pathway including rapid nucleation and growth towards a single crystal structure through diffusion of species from the solution to the initial nuclei surface.[61]

Sample	d_{TEM} (nm)	d_{core} (nm)	$<N_{core}>$	d_{XRD} (nm)	a (Å)	D_z (nm)	PDI	D_1 (nm)	D_2* (nm)
NF1	11.8 ± 3.5	11.8 ± 3.5	1.0	10.4 ± 1.1	8.365 ± 0.01	31	0.28	14.1	154 (25%)
NF2	16.4 ± 3.7	9.30 ± 1.6	2.2	16.9 ± 2.3	8.367 ± 0.003	31	0.21	17.7	49.4 (52%)
NF3	20.9 ± 3.6	10.0 ± 2.0	6.1	20.5 ± 9.7	8.385 ± 0.01	30	0.17	32.4	-
NF4	22.2 ± 4.1	11.6 ± 3.2	5.0	20.8 ± 3.5	8.371 ± 0.01	45	0.21	29.6	78 (47%)
NF5	23.1 ± 3.5	10.6 ± 2.0	8.0	17.7 ± 1.0	8.372 ± 0.01	32	0.20	24.0	192 (22%)
NF6	28.7 ± 4.9	8.80 ± 2.3	29.7	24.4 ± 4.9	8.368 ± 0.01	77	0.25	42.7	167 (47%)
NF7	29.3 ± 8.7	13.1 ± 4.2	9.1	22.0 ± 6.0	8.379 ± 0.01	82	0.20	59.1	150 (42%)

Table 1. Values of outer diameter and core size of NPs (d_{TEM} ; d_{core}) and number of cores $<N_{core}>$ determined by TEM image analysis, monocrystal size (d_{XRD}) and lattice parameter (a) determined by XRD analysis. The Z-average hydrodynamic diameter D_z and PDI are calculated with the Cumulant method, while D_1 and D_2 are given by Padé-Laplace algorithm (* respective weighing factor of the 2nd mode, in intensity).

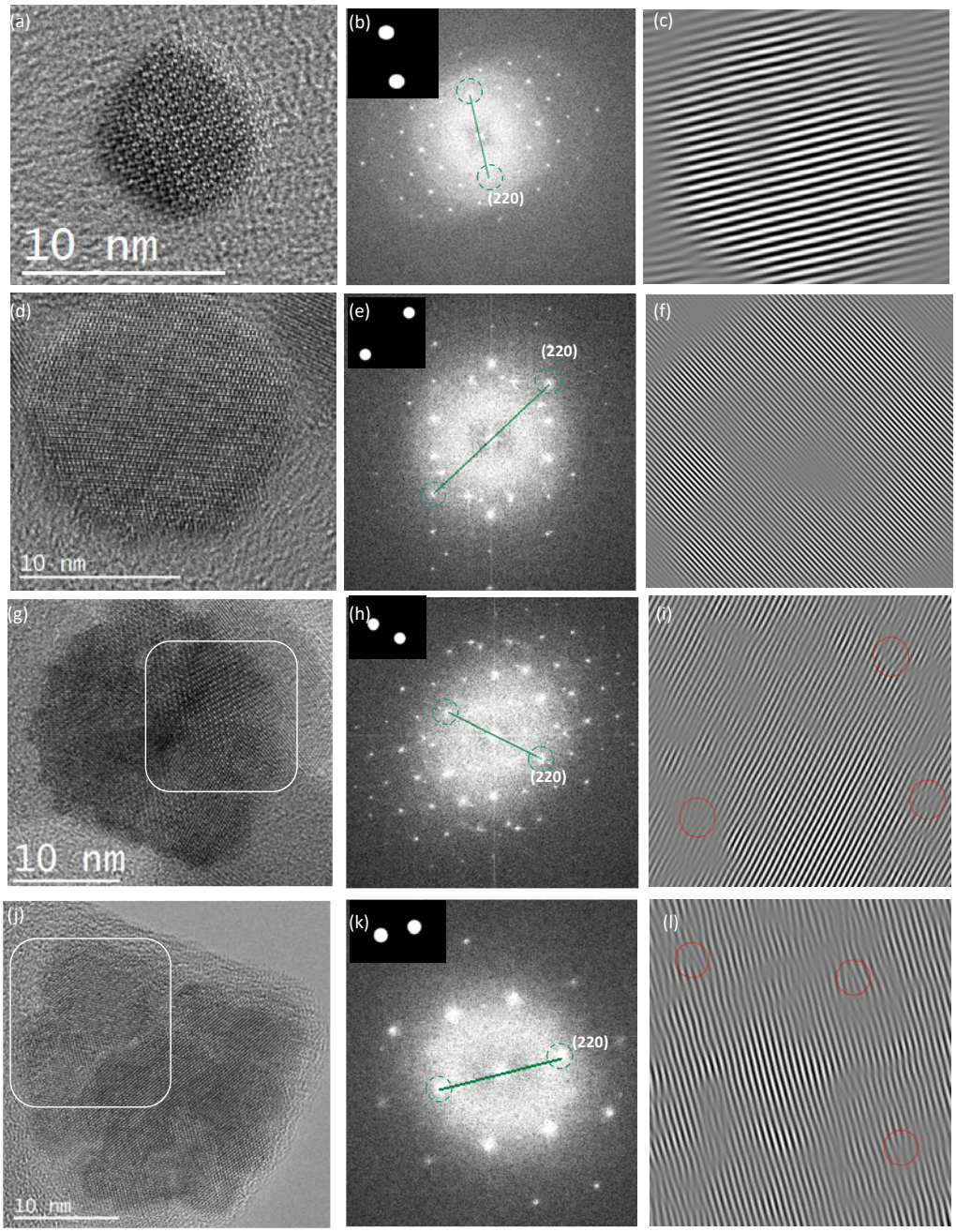

Figure 2. HR-TEM images of batches (a) NF1 (d) NF2, (g) NF4 and (j) NF6. (b),(e),(h) and (k) Fast Fourier Transformation (FFT) images obtained from HR-TEM images respectively. The inset shows the masking of the (220) planes in the FFT images. (c), (f), (i) and (l) are inverse FFT images of the (220) planes of NF1, 2, 4 and 6 selected in the FFT images respectively. Please note that (i) and (l) correspond to the zones depicted by the white squares in (g) and (j), respectively. Red circles depict the misalignments in (i) and (j).

3.2. Magnetic properties of the IONPs

3.2.1. Static magnetization measurements

Static magnetization experiments were performed on a vibrating sample magnetometer (VSM) at T=293 K in water after oxidation in order to determine their specific saturation magnetization M_s. The *M vs. H* curves under static field of all set of NPs are represented in **Figure 3**. It can be noticed that all the NF batches have M_s ranging from 300 up to 400 kA·m^{-1}, which are classical values for ferrite NPs (the bulk magnetization being 400 kA·m^{-1} for maghemite and 500 kA·m^{-1} for magnetite). Contrary to what is reported in literature for spherical IONPs,[64] the highest values of M_s (377 and 415 kA·m^{-1}), close to that of bulk γ-Fe_2O_3, was observed for the smallest samples (NF1 and 2 respectively). After closer investigation of M_s variation amongst samples, we noticed linear decrease with the proportion of multicore NPs and with the mean number of cores $<N_{core}>$ as shown in **Figure 3 (d)** and **S7** respectively.

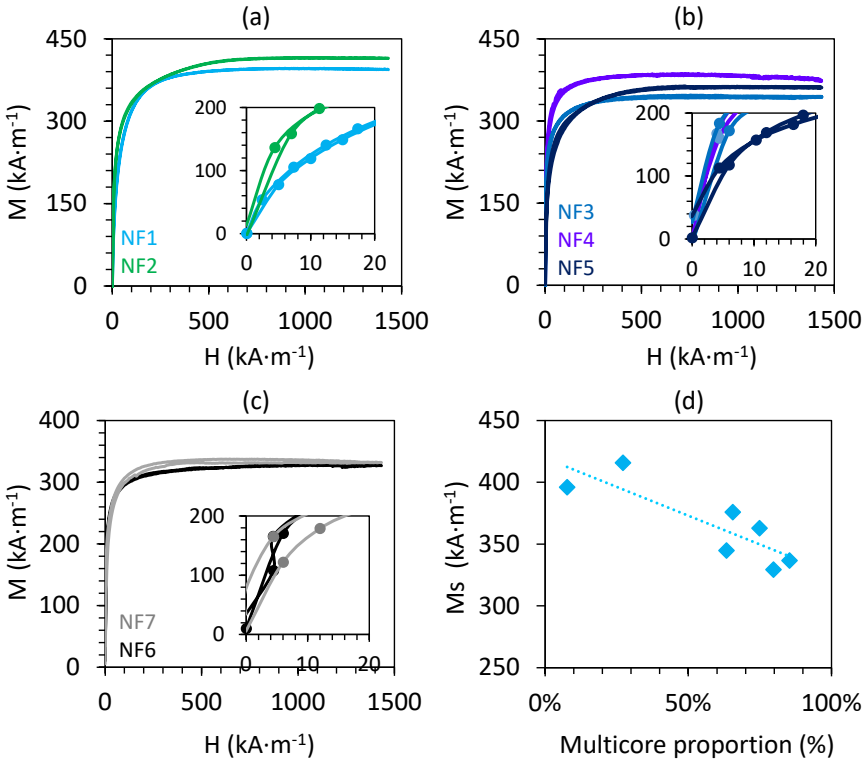

Figure 3. From (a) to (c): Magnetization curves of IONPs recorded at T=293K. The inset shows the magnetization of the NPs at low applied field. (d) Specific saturation magnetization M_s variation with flower-like NP proportion within the IONP batches.

As previously detailed, the spherical NPs possess lower number of defects in their crystal structure, contributing to higher M_s values, close to that of the bulk phase (case of NF1 and 2). On the other hand, the largest NPs possessing the highest multicore proportions exhibit the lowest M_s value (*i.e.* NF6 with the largest size and $<N_{core}>$ number) owing to higher occurrence of defects affecting the overall crystal integrity as aforementioned, inducing spin disorder. Our results follow the report of Levy *et al.*, as well as the recent study of Shingte *et al.*, which clearly demonstrate that lattice defects affect the magnetic moment magnitude and dynamics, resulting in lower magnetization and lower magneto-crystalline energy both for spherical and cubic morphologies.[38,71] In addition, we notice that the remnant magnetization M_r is negligible for batches NF1-6, confirming pure superparamagnetic behavior of the IONPs from 11.8 to 28.7 nm at room temperature as shown in the inset of **Figure 3 (a-c)**. On the opposite, sample NF7 of 29.3 nm diameter shows slight opening of the magnetization curve into a hysteresis loop characterized by a M_r of 81 kA·m^{-1} at 293 K and zero applied field. This indication of ferromagnetic contribution in the sample is either due to the presence of large NPs as evidenced by the size histogram in **Figure S1** or because, unlikely to all other flowerlike batches, its average grain size is significantly larger (d_{core}~13 nm as compared to d_{core} of 9-10 nm for all the other ones, including NF6).

For the NFs belonging to the superparamagnetic regime, the magnetization curves can be described by the Langevin function convolved with a Log-normal distribution of diameters, as shown below: [27]

$$M = M_S \int_0^\infty \delta d \cdot P_{d_0,\sigma}(d) \cdot L(\mu_0 \frac{M_d V_M}{k_B T} H_{app}) \qquad \text{Eq. (3)}$$

$$\text{with } P_{d_0,\sigma}(d) = \frac{1}{d \cdot \sigma \sqrt{2\pi}} \exp\left(\frac{-(\ln(d) - \ln(d_0))^2}{2\sigma^2}\right) \qquad \text{Eq. (4)}$$

Where μ_0 is the vacuum magnetic permeability, H_{app} the intensity of the applied field, M_d the magnetic domain magnetization, $V_M = \frac{\pi d^3}{6}$ the magnetic core volume for a spherical particle of diameter d, T being the absolute temperature and k_B the Boltzmann constant. Also, $P_{d_0,\sigma}(d)$ corresponds to the nanoparticle size distribution fitted by log-normal law where d_0 is the median value of the distribution and σ the standard width of the log values. The integral on diameters d is calculated numerically for a finite increment $\delta d = 0.1$ nm and only d_0 and σ as adjustable parameters (the domain magnetization being simply $M_d = M_s \cdot \rho$, where M_s is the saturation magnetization per mass of iron oxide and is $\rho = 4800$ kg·m^{-3} the mass density of the solid (taken as the tabulated value for maghemite). The results of fitted data are shown in **Figure S8** for all NFs.

From the Langevin fits on the experimental data of $M(H)$ and the specific relations of the log-normal law, we obtain the mean number-averaged magnetic size of the NPs:

$$d_{\mathrm{VSM}}^{\mathrm{n}} = d^{n} = \langle d \rangle = d_0 \exp\left(\frac{\sigma^2}{2}\right) \quad \text{Eq. (5)}$$

with its standard deviation: $Std(d) = d^{n}\sqrt{\exp(\sigma^2) - 1}$ Eq. (6).

The size distribution obtained by the Langevin fit can also be weighted by the volume fraction of the NPs expressed as $Phi(d) = P_{d_0,\sigma}(d) \cdot d^3$ (see histograms on **Figure S8**) to obtain the volume or weight-averaged magnetic diameter: $$d_{\mathrm{VSM}}^{\mathrm{w}} = d^{\mathrm{w}} = \langle \frac{d^4}{d^3} \rangle = d_0 \exp\left(\frac{7\sigma^2}{2}\right) \quad \text{Eq. (7)}$$

Table 2 gathers the obtained magnetic sizes at room temperature for all the set of NFs. For the smallest sample NF1, very small difference is found between d_{TEM}=11.8 nm, d^{w}=10.8 nm and d^{n}=9.3 nm. On the opposite, there is a notable shift between d^{w} and d^{n} for larger samples presenting higher proportions of multicore morphologies. For these samples (NF2 to 6), d^{n} values correspond, within experimental uncertainty, to sizes close to the small unit core diameters d_{core} as determined manually from TEM images. Moreover, for most samples the d^{w} values corresponding to the overall magnetic size of the multicore NPs are in good accordance with their outer diameter d_{TEM}, as well as with the crystal diameter d_{XRD}. Only for NF5 the d^{w} value is smaller than d_{TEM}. This can be ascribed to a possible dead magnetic layer around the magnetic monodomain. Another explanation could arise from the fact that, in electron microscopy, only a fraction of the IONPs (a few hundred) contribute to the histogram of diameters while in VSM, all the NPs in the sample (*i.e.* trillions) contribute to the final average values of the diameter.[51,72] Furthermore, the initial magnetic susceptibility χ at low applied field was determined for all the set of NF suspensions by taking the initial slope of the magnetization curves (see insets of **Figure 3** zooming in the region H_{DC}<25 kA·m^{-1}). The values, gathered in **Table 2**, are comprised between 15 and 40 and correspond to the very high χ range previously reported in the literature for IONFs.[31]

3.2.2. ZFC/FC curves and determination of the blocking temperature and anisotropy constant of the IONPs

ZFC/FC experiments were also conducted to determine the blocking temperature T_B as well as the effective magnetic anisotropy constant K_{eff} of the NPs, known as a determinant parameter for magnetic hyperthermia.[46] For this aim, samples with distinct outer TEM diameters of 11.8, 16.4, 20.9, 28.7 and 29.3 nm (NF1, 2, 3, 6 and 7) were selected. An aliquot of each batch of NPs was absorbed and dried in rectangular cotton pieces at low γ-Fe_2O_3 concentration to decrease as much as possible magnetic dipolar interactions between the IONPs by separating them with the cellulosic nanofibrils. In addition, the use of dried cotton pieces instead of common solvents to disperse the IONPs allows for the measurements to be conducted over a large range of T (from 100 K to 420 K) without observing the noise coming from the solvent melting point. The ZFC/FC curves shown in **Figure S9** and **S10** are characterized by two characteristic temperatures: at the maximum of the ZFC curve (T_{max}) as well as the

branching temperature (T_{bra}) where the ZFC and FC start shifting. At $T>T_{bra}$, the ZFC and FC curves superimpose as all particles relax, driven by thermal fluctuations.[73] Also, a shift of these two temperatures towards higher values was observed with the increase of the IONP outer size. Furthermore, for monodisperse IONPs, T_{max} corresponds to the blocking temperature T_B of the magnetic moments. However, this is not the case for these samples due to non-neglectable size distribution. In order to accurately estimate the average blocking temperature $<T_B>$, a method adapted for polysized samples reported by Micha *et al.* and Bruvera *et al.* was applied.[74,75] For this aim, the T derivative of the difference between ZFC and FC was plotted for each sample as shown in the **Figure S9** and **S10**. Then $<T_B>$ was determined from the maximum of the $\delta(M_{ZFC}-M_{FC})/\delta T$ plot. For the smallest samples mainly composed of spherical monocore IONPs (NF1 and 2), the presence of only one broad peak was observed and its maximum identified as the $<T_B>$ of these samples. On the other hand, for samples NF3, 6 and 7 composed mainly of multicore IONPs with sizes from 20.9 to 29.3 nm, up to 3 peaks appeared on the derivative plot, as illustrated in **Figure S9** (NF3) and **S10** (NF6-7). The presence of several peaks in the T dependence of the ZFC-FC derivative has already been reported for spherical or octopod-like morphologies[76], as well as for Fe_3O_4 or γ-Fe_2O_3 nanoflowers[31]. Based on these reports, we ascribed the broad intense peak (peak denoted as 1) to the IONP mean blocking temperature $<T_B>$. Two hypotheses can explain the presence of the additional peaks on the derivative curves of NF3, 6 and 7. The first cause could be contribution of the smallest NPs within the sample or the individual magnetic domains, inducing other blocking processes at T much lower than the average $<T_B>$ (peak noted 2 for NF6 and 7). The second hypothesis concerns the presence of magnetite within the largest IONPs, as evidenced previously by XRD and NIR optical absorption, giving rise to so-called Verwey transition at T_V close to 120 K for bulk magnetite. This insulator-conductor transition induces the appearance of an additional bump in the ZFC/FC curves as seen for NF3 and NF6 around 150 K (**Figure S9** and **S10**) and leads to the presence of a supplementary peak (noted 2 for NF3, and 3 for NF6 and 7) in the derivative curves. However, confirmation of these hypotheses require further experiments such as Mössbauer spectroscopy, EELS analysis, AC susceptibility *vs.* T etc., beyond the scope of this report. The values of the mean blocking temperature $<T_B>$ are gathered in **Table 2**. The $<T_B>$ of samples NF1 to 3 are in between 200-300 K, proving that the IONPs exhibit superparamagnetic behavior at ambient temperature. The large $<T_B>$ (>420 K) seen for sample NF7, was expected due to its ferromagnetic contribution as seen in the DC magnetization curve. Interestingly, the $<T_B>$ of NF6 is situated at 415 K, well above room temperature, even though its DC magnetization curve indicated a superparamagnetic behavior at 300 K. The large $<T_B>$ can thus be explained either from intra-particle interactions *i.e.* within the cores, enhanced for NF6 due to its high $<N_{core}>$ number, or from inter-particle *i.e.* dipolar interactions. The latter are less probable since very low IONP number density $C_{NP} = 2.4 \times 10^{12}$ NP·cm^{-3} was used for the ZFC/FC experiments, as explained in Materials & Methods section 2.3.8. Estimating the mean inter-particle distance $<r> = (3/(4\pi C_{NP}))^{1/3} = 465$ nm, the IONPs are

too distant for dipole-dipole interactions to have an effect.[77] Furthermore, the plotting of $<T_B>$ as a function of the overall magnetic domain size d^w shows linear dependency as illustrated on **Figure 4 (a)** (power law with exponent ~1). On the other hand, the plot of $<T_B>$ *versus* number $<N_{core}>$ of cores composing the IONPs shows progressive increase of $<T_B>$, following a power law with an exponent of 0.24 (**Figure 4 (b)**). It is known that $<T_B>$ increases with the size of the NPs. However, as previously mentioned, another contribution to large $<T_B>$ of multicore morphologies can arise from the presence of strong exchange coupling interactions between the cores, which favor high $<N_{core}>$ clusters with ferromagnetic order between the grains, a much rare behavior once coined by the term "superferromagnetism".[78]

From the value of $<T_B>$, the effective anisotropy constant K_{eff} was determined for each NP using the classical formula of the mean energy barrier: $\Delta E_{an}=25k_BT_B=K_{eff}V$ (k_B being the Boltzmann constant and V the magnetic volume deduced from d^w). The values of K_{eff} are gathered in **Table 2**. As expected, a fast increase of K_{eff} is observed towards small diameters as shown in the plot between K_{eff} and d^w in **Figure 4(c)**. This is due to higher contribution of surface anisotropy caused by the breaking of the symmetry and a reduction in the nearest neighbor coordination at the surface for smaller diameters.[79] However, when considering the magneto-crystalline energy barrier $\Delta E_{an}=K_{eff}V$ the highest value is obtained for the IONPs with d_{TEM}=28.7 nm, which is twice as large as the ΔE_{an} of sample NF1 (**Table 2**).On the other hand, K_{eff} progressively decreases with $<N_{core}>$ following a power law of exponent ≈0.5 as shown in **Figure 4(d)**.

By considering a simple approximation of spherical NPs with a diameter d, we can determine the surface and volume contribution to the effective anisotropy, as K_{eff} is given as the sum of volume and surface anisotropy contributions:

$$K_{eff} = K_V + (S\sigma/V)\,K_S = K_V + (6\sigma/d)K_S \qquad \text{Eq. (8)}$$

where $S = \pi d^2$ and $V = \pi d^3/6$ are the surface and the volume of the particle respectively, K_V the bulk anisotropy energy per unit volume, σ value measuring the deviation from a perfect sphere for which σ=1 and K_S the surface density of anisotropy energy.[79] The dependence between K_{eff} and the inverse of magnetic domain size ($1/d^w$) is linear as expected from the eq. above (inset **Figure 4 (d)**). From this, value of K_V=4.85 x 10^4 J·m^{-3} and K_S=2.5 x 10^{-4} J·m^{-2} were found for maghemite IONPs. K_V is one magnitude higher than the bulk anisotropy value of maghemite (4.6×10^3 J·m^{-3}) but agrees perfectly with reported values of K_V in literature for spherical maghemite NPs.[64,80,81,82,83] As for K_S, its value of is one magnitude higher than reported values of surface anisotropy for analogous spherical maghemite NPs (comprised between 2 - 4 $\times$ 10^{-5} J·m^{-2}). This can be ascribed to the highly corrugated morphology of IONFs which were shown by Hemery *et al* to exhibit much larger specific surface area (as measured in the wet state by small angle neutron scattering) as compared to perfectly smooth spheres of identical sizes.[31]

Furthermore, the anisotropy fields H_K calculated from $H_K=2K_{eff}/\mu_0 M_S$ were determined for all the set of samples and their values gathered in **Table 2**.

Sample	d^w (nm)	d^n (nm)	χ	M_S (kA·m^{-1})	$<T_B>$ (K)	K_{eff} (10^4 J·m^{-3})	ΔE_{ani} (10^{-20} J)	H_K (kA·m^{-1})
NF1	10.5	8.1	15.4	395.8	187	9.80	6.46	393.8
NF2	14.2	4.7	23.1	415.7	220	4.76	7.60	182.2
NF3	19.9	7.9	29.7	344.6	325	2.38	11.2	110.1
NF4	19.3	9.4	40.4	375.8	-	-	-	-
NF5	14.0	6.1	19.3	362.8	-	-	-	-
NF6	24.8	5.7	26.1	329.3	415	1.80	14.3	86.78
NF7*	-	-	19.3	336.5	>420	>6.89	>14.5	-

Table 2. Summary of weight-averaged VSM diameters d^w, number-averaged VSM diameters d^n, magnetic susceptibilities χ, specific saturation magnetizations M_S, blocking temperatures $<T_B>$, effective magnetic anisotropy constants K_{eff}, anisotropy fields H_K and anisotropy energy barriers ΔE_{ani} obtained through fitting of the DC magnetization curves obtained by vibrating sample magnetometry at room temperature, and analysis of zero-field cooled and field-cooled (ZFC/FC) curves from 100 K to 420 K under an applied bias field H_{DC}=4 kA·m^{-1}. *This sample exhibits slight magnetization hysteresis at room temperature.

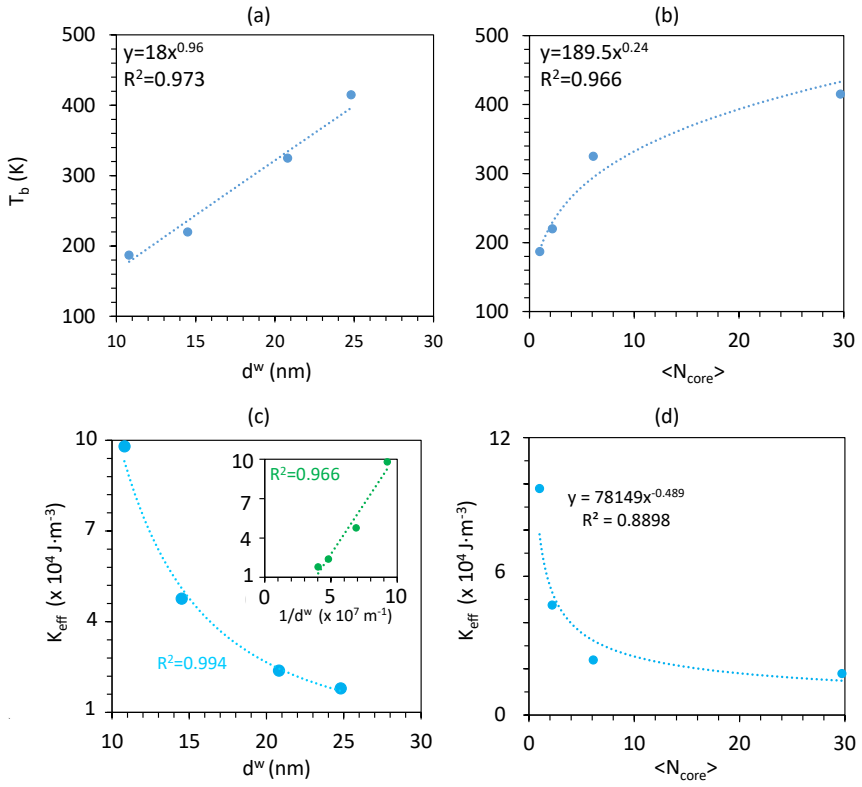

Figure 4. Scaling law determination between the magnetic parameters obtained by analysis of the ZFC-FC curves (blocking temperature and effective anisotropy constant) and the structural parameters (weight-average

diameter from the Langevin's fit of the VSM curve and number of cores calculated from the TEM diameters): Plots of (a) $<T_B>$ *vs.* d^w (b) $<T_B>$ *vs.* $<N_{core}>$ (c) K_{eff} *vs.* d^w with inset showing K_{eff} *vs.* $1/d^w$ and (d) K_{eff} *vs.* $<N_{core}>$.

3.2.3 Heat efficiency of IONPs evaluated through AC magnetization measurements

The heating efficiency of the IONPs was conducted *via* AC magnetometry experiments. This method was preferred when compared to classical calorimetry experiments to avoid errors rising from non-adiabatic conditions (thermal losses towards the environment) and to study several AMF conditions, within reasonable experimental time. In this case, an AC magnetic field is applied through a commercial resonant circuit (Nanotech Solutions, Madrid, Spain), inducing the rotation of magnetic moments of the NPs to follow the applied field but with a phase lag. This phase lag induces the opening of a dynamic hysteresis loop when plotting the instantaneous IONP magnetization M_t *vs.* the applied field H_t at time *t* recorded at a given frequency *f* and alternating magnetic field amplitude H_{max}.

In this case, the energy dissipated into heat by the NPs corresponds to the area *A* of the recorded hysteresis loop during one AMF cycle $T=2\pi/f$. The specific absorption rate (SAR) is the heat loss power normalized by the NPs' mass following the equation below:

$$\text{SAR}=\frac{\pi f}{c}A \qquad \text{with} \qquad A=\oint_{-H_{max}}^{+H_{max}} M_t \, dH_t \qquad \text{Eq. (9)}$$

where M_t is the instantaneous magnetization ($A\cdot m^{-1}$) at time *t*, H_t the field intensity ($A\cdot m^{-1}$) at time *t*, *f* (Hz) the applied magnetic field frequency and *c* ($kg\cdot m^{-3}$) the nanoparticle weight concentration of iron oxide in the dispersing medium (SAR is most often expressed in $W\cdot g^{-1}$ iron oxide or iron rather than $W\cdot kg^{-1}$).[40,51,37]

The larger the surface area *A* of the hysteresis loops, the larger the energy dissipated by the IONPs per AMF cycle and hence the SAR.[31] Curves showing the hysteresis loops and plots of SAR *vs.* H_{max} of NF1, 4 and 6 at different probed frequencies are gathered on **Figure 5**. The hysteresis loops as well as *A vs.* H_{max} and SAR *vs.* H_{max} for all set of NPs are found in SI (**Figures S11** to **S17**). An evolution of the loop shape with the size of the IONPs is observed, going from narrow (sample NF1) towards larger, more "open" and "square" loops (sample NF4 and 6) as seen in **Figure 5**. A power law fitting with an exponent varying from 1.5 to 2 of SAR *vs.* H_{max} curves is observed for all set of NPs. This nearly quadratic dependence $SAR\propto H_{max}^2$, as described by the Linear-Response Theory (LRT) also called "Rosensweig's model", indicates a superparamagnetic behavior of the synthesized IONPs batches.[84] Please note that the SAR *vs.* H_{max} curves of NF6 follows pure quadratic dependence with an exponent of ≈2, confirming once again its superparamagnetic character. On the other hand, for all set of NFs, the plots of *A vs*. H_{max} of each tested frequency, collapse onto a unique curve as shown in **Figures S11-17**. Area values as well as SAR of IONPs at two

field conditions (280 kHz, for 12 and 24 kA·m^{-1}) are gathered in **Table 3**. Until now, the highest area *A* per cycle reported in literature by Mehdaoui *et al.* is 11.2 mJ·g^{-1} for pristine Fe nanocubes of 13.7 nm size.[40]

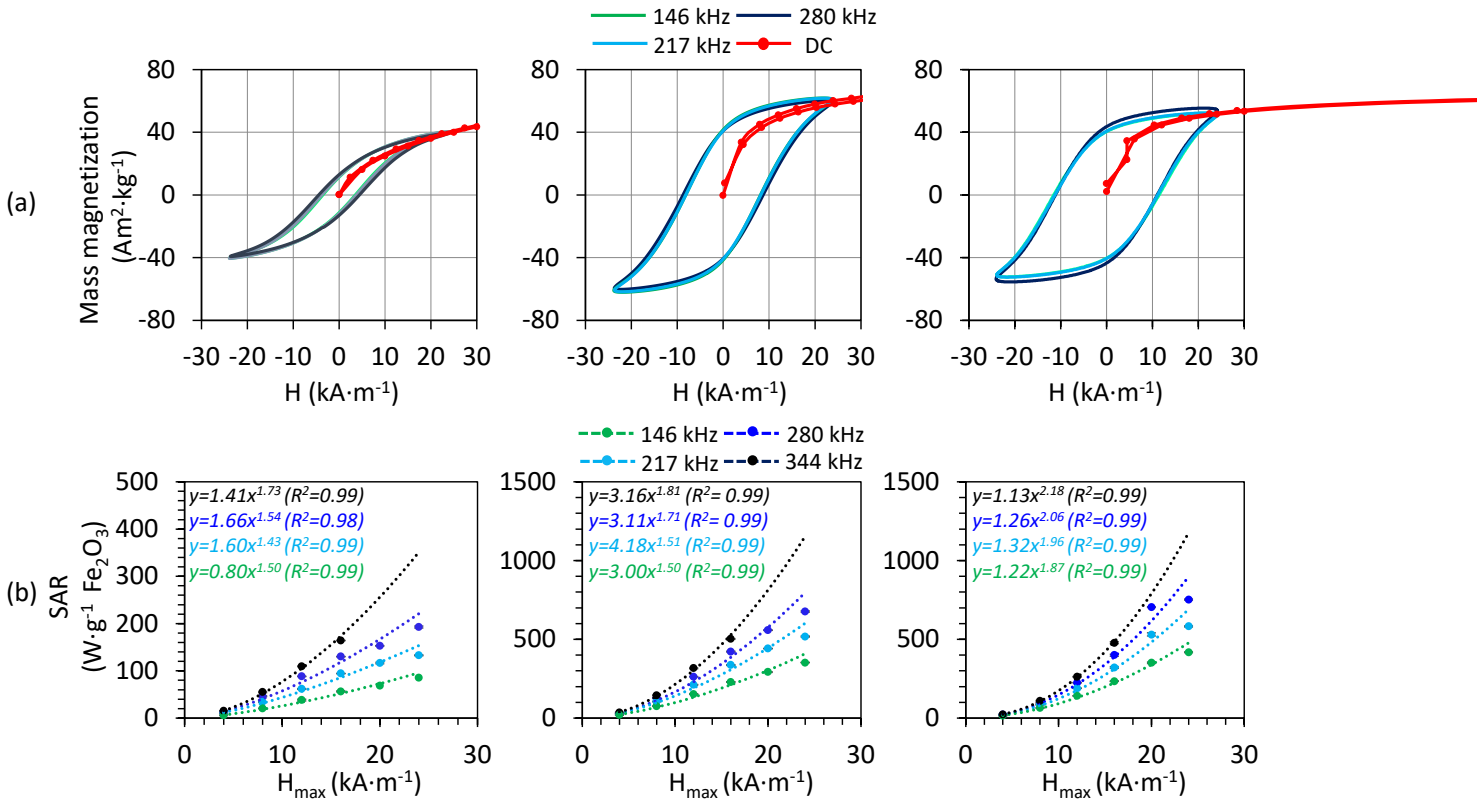

Figure 5. From left to right: Plots of (a) hysteresis loops at *f*=146, 217 and 280 kHz superimposed with the DC curve at low applied *H* and (b) SAR vs. H_{max} fitted with a power law of samples NF1, NF4 and NF6 respectively.

For the samples here made of iron oxide (that has advantage of chemical stability and biocompatibility compared to pristine iron), hysteresis area giving the loss per cycle reaches a value as high as *A*=2.70 mJ·g^{-1} for sample NF6 of 28.7 nm at *f*=280 kHz and H_{max}=24 kA·m^{-1}. This value is 1.5 times higher than the *A* value reported by Marciello *et al*. (*A*=1.83 mJ·g^{-1} at *f*=70 kHz and H_{max}=35 kA·m^{-1}) in their work of IONPs synthesis optimization for magnetic hyperthermia.[85] The SAR dependency plots on the external (TEM), the crystal and the magnetic monodomain diameters (d_{TEM}, d_{XRD}, d^w respectively) as well as <N_{core}> are gathered in **Figure 6** for four frequencies (146, 217, 280, 344 kHz) at H_{max}=12 (right row) and 24 kA·m^{-1} (left row) field amplitudes. As expected, the SAR values rise when increasing the AMF frequency or amplitude. When comparing the batches, the SAR increases monotonously with outer size d_{TEM}, crystalline size d_{XRD} and magnetic domain size d^w at high field amplitude (H_{max} >16 kA·m^{-1}) for all probed frequencies as shown in **Figure 6 (a-c)** for H_{max} = 24 kA·m^{-1} and **S18-S20** for H_{max}=20 kA·m^{-1}. More precisely, SAR increases progressively with d_{TEM}, d_{XRD} or d^w by following power laws of respective exponents *a* ≈

1.5-1.7, ≈1.6-1.9 and 1.5-1.8 when *f* varies from 146 to 280 kHz and for H_{max} >16 kA·m^{-1}. Furthermore, the best fit is obtained (*i.e.* with the closest coefficients of determination R^2 to 1) when plotting SAR *vs.* d_{XRD}, with SAR continuously increasing with the crystal size for H_{max} >16 kA·m^{-1}.

	H_{max}=24 kA·m^{-1}		H_{max}=12 kA·m^{-1}	
Samples	*A* (mJ·kg^{-1})	SAR (W·g^{-1})	*A* (mJ·kg^{-1})	SAR (W·g^{-1})
NF1	693.2 ± 3.0	192.7 ± 0.8	316.9 ± 1.3	88.2 ± 0.3
NF2	1320 ± 14	430.0 ± 3.3	679.1 ± 10.1	189.1 ± 2.7
NF3	2266 ± 22	639.0 ± 6.2	923.8 ± 10.9	257.2 ± 3.0
NF4	2430 ± 17	676.2 ± 4.7	944.3 ± 2.8	262.8 ± 0.7
NF5	1700 ± 8	473.2 ± 2.1	789.1 ± 5.6	219.7 ± 1.5
NF6	2700 ± 17	751.3 ± 4.7	804.7 ± 1.9	224.2 ± 0.5
NF7	2076 ± 29	578.1 ± 8.20	695.9 ± 6.8	193.7 ± 1.9

Table 3. Values of hysteresis loop area *A* and SAR expressed in mJ·kg^{-1} and W·g^{-1} Fe_2O_3 respectively, recorded at 280 kHz for H_{max}=12 and 24 kA·m^{-1} for all the set of IONPs.

On the other hand, when analyzing the plot of SAR *vs.* d_{TEM}, it reaches a maximum of 751 W·g^{-1} Fe_2O_3 at d_{TEM}=28.7 nm and then slightly decreases down to 575 W·g^{-1} Fe_2O_3 at *d*=29.3 nm (sample NF7) at 280 kHz and 24 kA·m^{-1}. The slight decrease of SAR is observed for each probed frequency and can be ascribed to loss of the superparamagnetic properties at *d*≈30 nm when the NPs start exhibiting ferromagnetic behavior as shown previously in the DC magnetization curves of NF7 (**Figure 3(c)**). Another explanation can be the lower crystalline size of sample NF7 as compared to NF6. On the other hand, when comparing the three analogous samples NF3, NF4, NF5, synthesized using identical polyol conditions, a slight decrease of SAR from 639 and 676 W·g^{-1} Fe_2O_3 (NF3 and NF4 respectively) to 473 W·g^{-1} Fe_2O_3 for NF5 was observed at 280 kHz and 24 kA·m^{-1}. It is worth noticing that among the three analogous samples, NF5 has the lowest crystalline and magnetic domain sizes, which undoubtedly affects its heating properties.

Interestingly, the nearly parabolic increase of SAR *vs.* d_{TEM}, d_{XRD} and d^w is lost at lower field amplitudes at almost all probed frequencies (R^2 too low when fitting with a power law; dashed line in **Figure 6 (b), (d)** and **(f)** for 12 kA·m^{-1} is given as guide for the eye), accompanied by decrease of spread of SAR values among the samples as illustrated in **Figure 6 (b) (d)** and **(f)**. Furthermore, depending on the probed frequency, the appearance of new size optima for which SAR reaches a maximal value at low field amplitude was noticed. For instance, at *f*=146-344 kHz and for H_{max}=12-16 kA·m^{-1}, the optimal size is d_{TEM}=22.2 nm (d_{XRD}=20.8 nm; d^w=19.5 nm) corresponding to the sample NF4 as shown in **Figure 6 (b), (d)** and **(f)** for 12 kA·m^{-1} and **Figure S18-20 (b)** for 16 kA·m^{-1}.

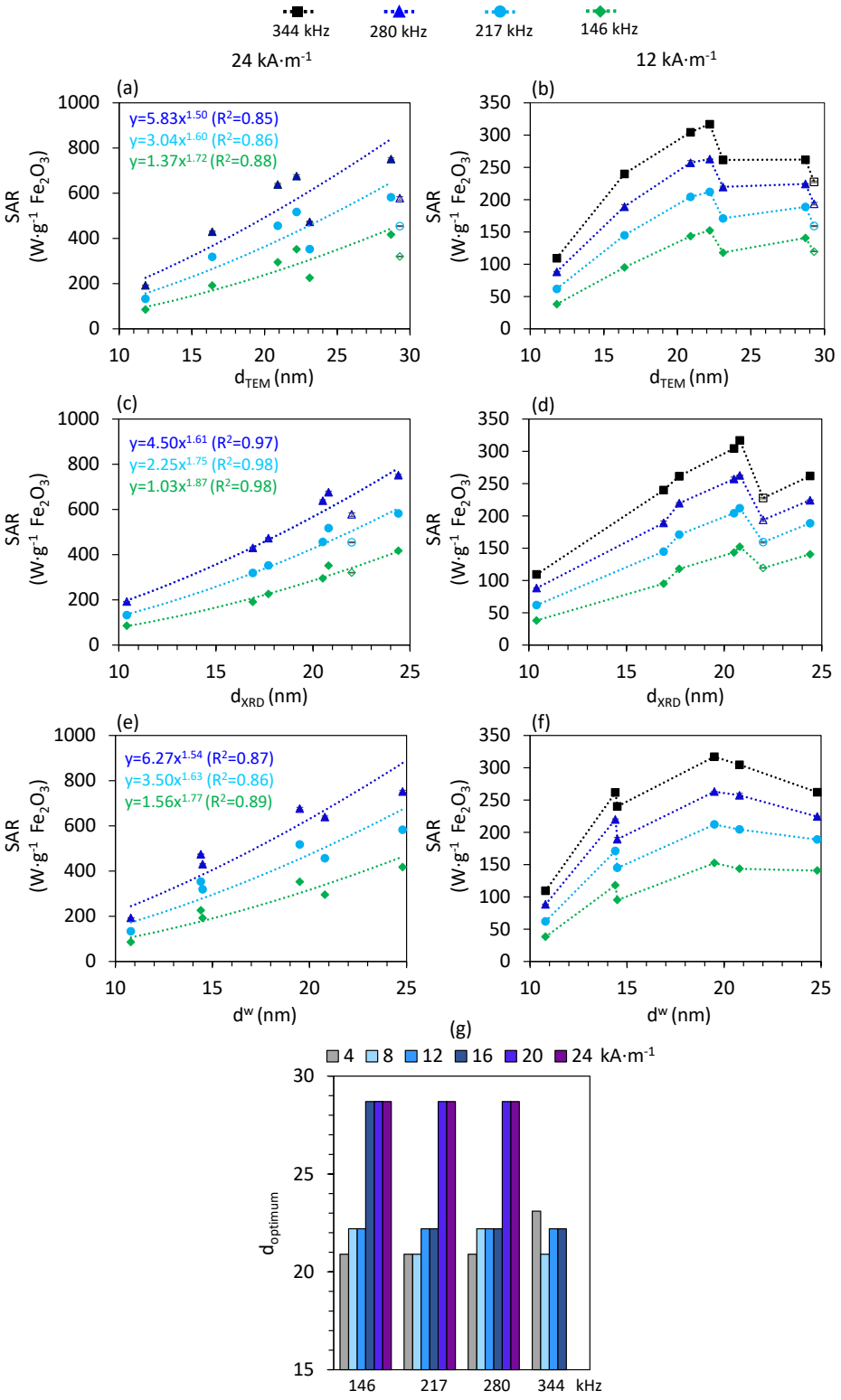

Figure 6. (a-b) SAR variation with outer size (d_{TEM}), (c-d) crystalline size (d_{XRD}) or (e-f) magnetic domain size (d^w) probed at H_{max}=24 kA·m^{-1} (left column) and 12 kA·m^{-1} (right column). Please note the linearity loss as well as the appearance of a new SAR maximum for d_{opt}=22.4 nm. (g) Variation of d_{opt} with the applied field amplitude H_{max} at

all probed frequencies. Please note that the unfilled data points correspond to sample NF7, presenting ferromagnetic contribution.

Similarly, for f=217 and 344 kHz, the optimum size shifts from d_{TEM}=22.4 nm at H=12-16 kA·m^{-1} to d_{TEM}=20.9 (d_{XRD}=22.7 nm; d^{w}=20.8 nm) and then at 23.3 nm (d_{XRD}=17.7 nm; d^{w}=14.4 nm) at 8 kA·m^{-1} (**Figure S18-20 (c)**) and 4 kA·m^{-1} (**Figure S18-20 (d)**) respectively. **Figure 6 (g)** represents the evolution of the optimum size (d_{opt}) taken from the SAR *vs.* d_{TEM} variation curves, with the maximum applied field H_{max} at all probed frequencies. A general trend is observed with d_{opt} shifting towards higher values when increasing the applied field amplitude H_{max}. The shifting of d_{opt} with the applied AMF amplitude has recently been reported by the theoretical study of Engelmann *et al.*, where they use Monte Carlo (MC) simulations to predict the heating power of iron oxide NPs. [54,55] The SAR dependence with the size of the NPs, as predicted by these MC simulations follows tendencies similar to our experimental results. For instance, when considering K_{eff}=11 kJ·m^{-3} as effective anisotropy constant for MC simulations, Engelmann *et al.* found a Gaussian-like dependency of the SAR *vs.* NP diameter curve, for both H_{max}=16 and 5 kA·m^{-1} at 176 kHz. In addition, these authors report a shift of the d_{opt} from 18 to 22 nm when rising the field H_{max} from 5 to 16 kA·m^{-1} at 176 kHz. Their MC simulations match quite well our results, as we experimentally observe curves displaying maxima for H<16 kA·m^{-1} as well as a shift of d_{opt} from 20.9 to 22.2 nm when the field amplitude increases from 4 to 12 and 16 kA·m^{-1} at 146 kHz as shown in **Figure 6 (g)** and **S18 (c-d)** for 146 kHz (green curve). There is also similarity between the range of SAR values predicted by the MC simulations and the experimental values of the present study. On the other hand, Mehdaoui *et al.* attributed the shift of d_{opt} size of pristine Fe nanocubes when increasing the magnetic field as a natural consequence of theory derived from the 2-state Stoner-Wohlfarth model where the maximum area A is obtained for an optimal coercive field, situated slightly below H_{max} and related to the particle volume V and applied magnetic field amplitude H_{max} as follows[40]:

$$\mu_0 H_{\max} \gtrsim \mu_0 H_c = 0.48 \mu_0 H_K (1 - k^{0.8}) \qquad \text{Eq. (10)}$$

H_K being the anisotropy field ($H_K = \frac{2K_{eff}}{\mu_0 M_s}$) and k = ($\frac{k_B T}{K_{eff} V}$) ln($\frac{k_B T}{4\mu_0 M_s H_{max} \tau_0 V}$), τ_0 is the frequency factor of Néel's relaxation time.

Optimum conditions for maximal A happen when H_c is close to H_{max}. Thus, for an increasing field, optimal conditions are created for larger H_c, which is obtained at higher particle volume V (higher V decreases k). This explains the increase of d_{opt} at higher field amplitudes, for given frequency, within the Stoner Wohlfarth model. Inspired from the recent work of Bertuit *et al.*, we studied the evolution of SAR with the number of cores composing the NFs. The mean core size remaining similar over all the set of NFs enables to compare how <N_{core}> affects the heating efficiency among the samples. The curves of SAR *vs.* <N_{core}> are shown in **Figure 7 (a-b)** for

H_{max}=24 and 12 kA·m^{-1} as well as **Figure S21 (a-d)** for all the other probed AMF conditions. As shown in **Figure 7 (a)**, the SAR starts to increase linearly with <N_{core}> but passed a local peak near <N_{core}>= 5-6, the SAR starts to go down for larger <N_{core}> values up to ~10, and then it is only at much higher value <N_{core}>~30 that the SAR starts to rise again, for all probed frequencies. Under these conditions, the highest SAR value is systematically obtained for the highest <N_{core}>=29.7 corresponding to NF6. These results correspond well with the report of Bertuit *et al.* where the highest SAR was obtained for the largest <N_{core}>=23 at H_{max}=14.3 kA·m^{-1} and f=471 kHz. But contrary to our result, their evolution of SAR with <N_{core}> at H_{max}=14.3 kA·m^{-1} and f=471 kHz remained perfectly linear even at high <N_{core}>. [47] This linear correlation between SAR and <N_{core}> was attributed to the exchange couplings between the cores that are enhanced at high <N_{core}> and as consequence improve the heating power of the NPs. In this report, the evolution of SAR with <N_{core}> was examined at various frequencies and field amplitudes. We observe that when the field amplitude decreased H_{max}<16 kA·m^{-1}, the plot of SAR *vs.* <N_{core}> increases linearly up until reaching a new SAR maximum for <N_{core}>= 5.0 corresponding to NF4 sample and then slightly decreasing at larger <N_{core}>. This tendency was observed at all probed frequencies for H_{max}=4-16 kA·m^{-1} (**Figure 7(b)**) and **Figure S21 (c-d)**. Similarly, to d_{opt}, the optimum <N_{core}>, corresponding to the highest SAR value, shifts towards higher values when increasing the magnetic field amplitude H_{max}.

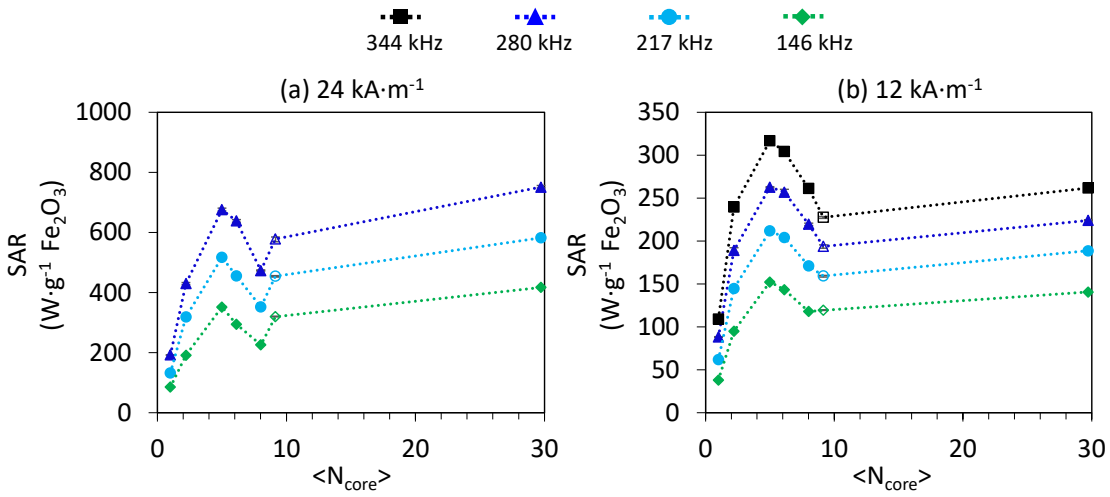

Figure 7. SAR evolution with <N_{core}> for four frequencies at (a) H_{max}=12 and (b) H_{max}=24 kA·m^{-1}.

In addition to SAR, the evolution of the hysteresis loop "squareness" with <N_{core}> of the NFs was also investigated. The "raw" plots of the hysteresis loop superimposed in the order of increasing <N_{core}> of our samples for H=24 kA·m^{-1} at f=280 kHz is given in **Figure 8 (a)** (raw and normalized curves of hysteresis loops at H=4-20 kA·m^{-1} at f=280 kHz are found in **Figure S22**). As it can be seen, although the overall shape of the hysteresis loop remains similar within the different IONPs, the loop "opens up" towards more "square-like" shape when increasing <N_{core}>.

Please notice how the sample NF6 which possesses the highest <N_{core}> systematically has the largest coercive fields H_c, hence the most "open" loop at all applied fields, as illustrated in the normalized hysteresis plots (see **Figure S22 (b)**, **(d)** and **(f)**).

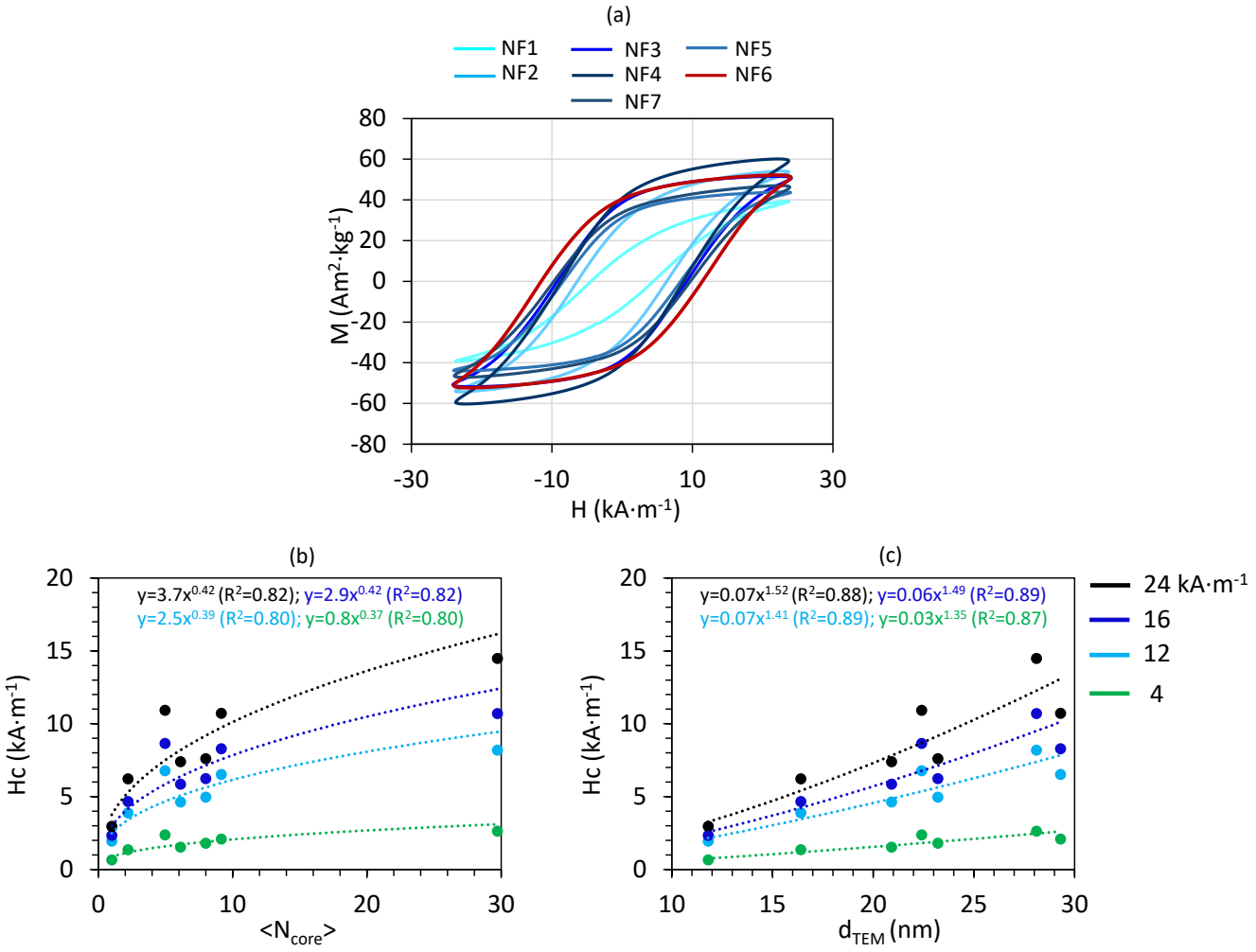

Figure 8. (a) Superimposed hysteresis cycles of NF1-7 at 24 kA·m^{-1} and 280 kHz. (b) and (c) Evolution of the coercive field H_c of IONPs *vs.* the core number <N_{core}> and the diameter d_{TEM} respectively. At all applied fields, the sample having the largest number of grains (NF6) exhibits the highest H_c.

To better illustrate this tendency, the graphs of H_c *vs.* <N_{core}> and H_c *vs.* d_{TEM} were plotted on **Figure 8 (b-c)**. It is noticeable that the coercive field follows linear increase with d_{TEM}. On the other hand, H_c increases with <N_{core}> following a power law of exponent ~0.40, therefore the highest H_c is reached for the highest <N_{core}> (sample NF6) at all applied fields. The increase of H_c with the particle diameter and <N_{core}> is related to an overall increase of the anisotropy barrier when increasing the size, as well as interactions between cores that rise at larger <N_{core}>

values. Therefore, a higher applied field is needed to reverse the magnetization of larger NPs with enhanced intra-particle interactions. Contrary to the variation of SAR plotted *vs.* $<N_{core}>$, the H_c *vs.* $<N_{core}>$ and H_c *vs.* d_{TEM} graphs display the same monotonous increase tendencies under all conditions of the applied magnetic field.

4. Discussion

In this paper, the relationship between structural and magnetic properties of IONPs produced *via* simple polyol route were investigated. IONPs within the size range of 10 and 30 nm were prepared by slightly modifying the original polyol conditions firstly introduced by Caruntu *et al*. We noticed that when inducing faster nucleation of NPs by either adding H_2O or increasing the content of DEG in the polyol medium, decrease of the overall size and morphology change of the NPs from multi to monocore NPs were induced. However, when using classical polyol conditions, the synthesized IONPs exhibited both morphologies – mono and multicore – the latter being the predominant morphology. SAED and XRD diffraction patterns coincide well with the tabulated peaks for magnetite and maghemite. The cell parameter deduced from XRD pattern refinement are found to be in between magnetite and maghemite for all our samples. The oxidation of the NPs, being a size-dependent step as previously reported, it is most-likely incomplete, inducing the presence of magnetite within the NPs. The presence of magnetite within the samples was confirmed through Visible-NIR absorbance spectrum where the NIR band, corresponding to IVCT of magnetite, increased with the size of the NP, indicating higher proportion of magnetite for the largest samples. The presence of magnetite was also seen on the ZFC/FC curves through the Verwey transition occurring at T≈150-120 K on the largest tested samples (NF3 and 6). Besides the composition, the structural defects are known to affect the magnetic properties of IONPs. Thus, structural defects were evidenced by performing the FFT treatment on the HR-TEM images. A difference was seen amongst our samples: NF1 and 2 composed mainly by spherical monocore NPs with little to no defects among the studied planes whereas NF3-NF6 composed mainly by multicore NPs present zones rich in misalignments along (220), (311), and (211) planes, as shown in **Figure S5**. The presence of defects within the multicore NPs was confirmed through fluorescence spectroscopy, where intense emission was observed for multicore NPs, with the luminescence intensity increasing with their size, $<N_{core}>$ and more interestingly with the outer surface area ($\propto d_{TEM}^2$), as a result of higher defect concentration.[47] This atomic disorder directly influences the specific saturation magnetization of the NPs: their M_S value decreases with the multicore NP proportion as well as the number $<N_{core}>$, despite the overall size increase of the IONPs, due to the loss of the crystal integrity with the presence of defects, and the surface disorder as well. Furthermore, when comparing samples NF3, 4 and 5 synthesized under identical conditions and with similar d_{TEM} and M_S, NF5 displays the lowest heating efficiency amongst them. The main difference within these samples is the mean magnetic diameter, which for NF5 is quite low when compared to its overall diameter (d_{TEM}=23.1 nm, d^w=14.2 nm) and similar to that of NF2

(d_{TEM}=16.4 nm, d^{w}=14.5 nm). With distinct outer diameters but very similar magnetic domain size, these two samples have very similar heating efficiencies under all probed AMF conditions, despite the higher <N_{core}> of NF5. In this case, we relate the lower heating efficiency of NF5 compared to its analogous samples NF3 and 4, as a direct consequence of a lower magneto-crystalline energy barrier ΔE_{ani}, due to the small magnetic volume. This also explains why, the samples NF2 and 5 with distinct core diameters but similar magnetic domain and crystal sizes have similar heating properties. In addition, NF6 and 7, which are also synthesized under identical polyol conditions, do not have the same properties despite their close diameters (28.1 nm for NF6 and 29.3 nm for NF7). For instance, NF7 exhibits a lower crystal size, <N_{core}> and a ferromagnetic behavior, when compared to NF6, all in detriment to its heating properties. The comparison between these two sets of analogous NPs clearly demonstrates that classic polyol route offers a good reproducibility of NPs in terms of overall diameter and morphology *i.e.* mono or multicore, however lacks control on the structural features that directly affect the heating efficiency of IONPs (*i.e.* crystal and magnetic size, <N_{core}>, size-distribution etc.). The low yield, the high energy consuming synthesis alongside with the lack of control of NPs' intrinsic properties affecting their SAR represent the main drawbacks of the polyol route. Solutions to these issues in the near future, may involve the use of novel polyol reactors *i.e.* milli-fluidic reactors, which allow for a better control of the final physicochemical properties of IONFs as well as their large-scale production as recently reported.[86]

Besides structural parameters, we also bring proof that the heating efficiency of IONPs is tightly related to the applied magnetic field conditions as well. Firstly, the *SAR* of all the IONPs, evaluated at various AMF conditions, varies as H_{max}^{2}, as predicted by the LRT theory for superparamagnetic NPs. Secondly, its simultaneous dependence with size and magnetic field can be summarized by considering two regimes: 1/ High field amplitude regime for H>16 kA·m^{-1} where the d_{opt} giving the highest SAR is 28.7 nm corresponding to the sample having the highest crystal, magnetic domain size and <N_{core}>; 2/ Low field amplitude regime H<16 kA·m^{-1} where the d_{opt} shifts to 22.4 or to 20.9 nm depending on the applied field. Furthermore, the evolution of *SAR* with <N_{core}> is also dependent of the field conditions. For instance, under high field amplitude regime, the highest *SAR* corresponds to the sample NF6 of 28.7 nm with the highest <N_{core}>, which can be explained as a consequence of its high magnetic domain size (close to its crystal size) as well as enhanced exchange interactions at high <N_{core}> as recently reported by Bertuit *et al.*[47] In our study, we clearly demonstrate that the evolution of *SAR* with <N_{core}> deviates when decreasing the field by showing new *SAR* optimum at lower <N_{core}>. This completes the result of Bertuit *et al.* where the *SAR* linearity with <N_{core}> was demonstrated under only one AMF condition *i.e.* 14 kA·m^{-1} and 471 kHz. Moreover, following the predictions of Stoner-Wohlfarth model, our d_{opt} increases with field amplitude whereas the H_c increases with the size and <N_{core}> of the NPs under all applied AMF conditions. Mehdaoui *et al.*, reported very similar results to ours for pristine Fe nanocubes, where they experimentally observed an increase of the

coercive field with the size of the NPs as well as the increase of d_{opt} with the amplitude of the magnetic field. The experimental results were explained within the Stoner Wohlfarth model, adapted for NPs in the ferromagnetic regime with uniaxial anisotropy. On the other hand, Monte Carlo simulations for SAR prediction on superparamagnetic spherical iron oxide more similar to our NPs, report the same tendencies: 1/ sigmoidal increase of SAR with size at high field amplitudes or first an increase of SAR then decrease for small field amplitudes giving rise to d_{opt}; 2/ shift of d_{opt} when increasing the magnetic field amplitude.[33,55,54] This kind of SAR dependence with the magnetic field and size can be explained by taking in account the anisotropy field of the NPs, H_K. In our case, due to the high anisotropy of the NPs the applied field remains too small compared to H_K, signifying that the heating contribution is of superparamagnetic behavior. Thus, increasing the particle diameter *d* leads to the suppression of thermal activation due to the particle moment blocking, and as a result SAR decreases after d_{opt}.[87] Furthermore, like LRT, the MC simulations of the aforementioned studies, predict a variation of SAR $\propto H^2$ for $H<<H_K$, which is observed in the case of all our IONPs. The increase of the d_{opt} with the magnetic field is also predicted within the Monte-Carlo simulations, however a clear physical explanation of this phenomenon was not found and up to know it has been explained through Stoner Wohlfarth model.[40] The results presented in this report suggest that the choice of the IONPs for biomedical applications should be adapted with the used magnetic field conditions. For instance, in order to be below the clinical "Brezovitch's limit" ($H \times f < 5 \times 10^9$ A·m^{-1}·s^{-1})[88], two choices for the AMF conditions are possible: low field amplitude and high frequency *i.e* 280-344 kHz for H<16 kA·m^{-1} or high field amplitude and low frequency *i.e.* 146-217 kHz for H>16 kA·m^{-1}. In our case, the NPs of 22.2 nm would be the best candidates for the first conditions whereas the NPs of 28.7 nm for the second. In both cases, the maximum SAR reached is within 400-500 W·g^{-1} Fe_2O_3, which corresponds to suitable values for biomedical applications, where the injected dose of magnetic NPs is to be minimized.

5. Conclusion

The extensive investigation of structural, magnetic properties of IONPs, and their impact on the heating efficiency has allowed us to draw the conclusions below: 1/ Structural defects present within the multicore morphologies affect the saturation magnetization of the NPs. 2/ When comparing analogous IONPs, the highest SAR is systematically obtained for the IONPs having a magnetic size close to its crystal and physical diameter. 3/ Intra-particle exchange interaction between the cores drive the $<T_B>$ towards high values, and thus increase the overall magneto crystalline energy barrier ΔE_{ani} of the NPs. On the other hand, $<N_{core}>$ is not the only parameter affecting the SAR of the NPs. 4/ SAR is a complex parameter depending simultaneously on structural features (magnetic, crystalline, or overall diameter, $<N_{core}>$ number and atomic defects) and the applied magnetic field conditions. Herein, the experimental results clearly demonstrate that the magnetic field can drive the SAR of NPs and induce

the appearance of SAR maxima at optimum diameters. The optimum diameters are also dependent on the amplitude of the magnetic field, where their shift was recorded with the increase of H_{max}. 5/ The heating properties of the IONFs seem to lie in between known theoretical models *i.e.* LRT (with SAR $\propto H^2$) and Stoner-Wohlfarth (with d_{opt} and H_c increasing with H_{max} and size of the NPs, respectively). Our experimental results fit at best with aforementioned studies that consider MC simulations with no theoretical limitations in contrast to the LRT (d_{NP}<10 nm) and the Stoner-Wohlfarth "two-state model" (ferromagnetic NPs) for particle heating predictions.[54,55] To our knowledge, such comprehensive experimental study for iron oxide nanoflowers has not been reported before.

SUPPLEMENTAL INFORMATION

Additional measurements (TEM size histograms, SAED and XRD patterns, absorption and fluorescence spectra, DC magnetization curves, AC hysteresis loops and various other plots) are provided in the supplemental information file that can be downloaded at the publisher's website.

DATA AVALAIBILITY

Whenever needed for comparison to other experimental results or theoretical fitting, the raw data of all graphs of this study are freely available on the Zenodo.org public repository (DOI: 10.5281/zenodo.7596848)

REFERENCES

(1) Ko, M. J.; Hong, H.; Choi, H.; Kang, H.; Kim, D.-H. Multifunctional Magnetic Nanoparticles for Dynamic Imaging and Therapy. *Adv. NanoBiomed Res.* **2022**, *2* (11), 2200053. https://doi.org/10.1002/anbr.202200053.

(2) Ma, Z.; Mohapatra, J.; Wei, K.; Liu, J. P.; Sun, S. Magnetic Nanoparticles: Synthesis, Anisotropy, and Applications. *Chem. Rev.* **2021**. https://doi.org/10.1021/acs.chemrev.1c00860.

(3) Dadfar, S. M.; Roemhild, K.; Drude, N. I.; von Stillfried, S.; Knüchel, R.; Kiessling, F.; Lammers, T. Iron Oxide Nanoparticles: Diagnostic, Therapeutic and Theranostic Applications. *Adv. Drug Deliv. Rev.* **2019**, *138*, 302–325. https://doi.org/10.1016/j.addr.2019.01.005.

(4) Yoon, T.-J.; Lee, H.; Shao, H.; Weissleder, R. Highly Magnetic Core–Shell Nanoparticles with a Unique Magnetization Mechanism. *Angew. Chem. Int. Ed.* **2011**, *50* (20), 4663–4666. https://doi.org/10.1002/anie.201100101.

(5) Maier-Hauff, K.; Ulrich, F.; Nestler, D.; Niehoff, H.; Wust, P.; Thiesen, B.; Orawa, H.; Budach, V.; Jordan, A. Efficacy and Safety of Intratumoral Thermotherapy Using Magnetic Iron-Oxide Nanoparticles Combined with External Beam Radiotherapy on Patients with Recurrent Glioblastoma Multiforme. *J. Neurooncol.* **2011**, *103* (2), 317–324. https://doi.org/10.1007/s11060-010-0389-0.

(6) Mertz, D.; Sandre, O.; Begin-Colin, S. Drug Releasing Nanoplatforms Activated by Alternating Magnetic Fields. *Biochim. Biophys. Acta BBA - Gen. Subj.* **2017**, *1861* (6), 1617–1641. https://doi.org/10.1016/j.bbagen.2017.02.025.

(7) Cazares-Cortes, E.; Espinosa, A.; Guigner, J.-M.; Michel, A.; Griffete, N.; Wilhelm, C.; Ménager, C. Doxorubicin Intracellular Remote Release from Biocompatible Oligo(Ethylene Glycol) Methyl Ether Methacrylate-Based Magnetic Nanogels Triggered by Magnetic Hyperthermia. *ACS Appl. Mater. Interfaces* **2017**, *9* (31), 25775–25788. https://doi.org/10.1021/acsami.7b06553.

(8) Chen, W.; Cheng, C.-A.; Zink, J. I. Spatial, Temporal, and Dose Control of Drug Delivery Using Noninvasive Magnetic Stimulation. *ACS Nano* **2019**, acsnano.8b06655. https://doi.org/10.1021/acsnano.8b06655.

(9) Mai, B. T.; Balakrishnan, P. B.; Barthel, M. J.; Piccardi, F.; Niculaes, D.; Marinaro, F.; Fernandes, S.; Curcio, A.; Kakwere, H.; Autret, G.; Cingolani, R.; Gazeau, F.; Pellegrino, T. Thermoresponsive Iron Oxide Nanocubes for an Effective Clinical Translation of Magnetic Hyperthermia and Heat-Mediated Chemotherapy. *ACS Appl. Mater. Interfaces* **2019**, *11* (6), 5727–5739. https://doi.org/10.1021/acsami.8b16226.

(10) Caruntu, D.; Caruntu, G.; Chen, Y.; O'Connor, C. J.; Goloverda, G.; Kolesnichenko, V. L. Synthesis of Variable-Sized Nanocrystals of Fe_3O_4 with High Surface Reactivity. *Chem. Mater.* **2004**, *16* (25), 5527–5534. https://doi.org/10.1021/cm0487977.

(11) Banfield, J. F.; Welch, S. A.; Zhang, H.; Ebert, T. T.; Penn, R. L. Aggregation-Based Crystal Growth and Microstructure Development in Natural Iron Oxyhydroxide Biomineralization Products. *Science* **2000**, *289* (5480), 751–754. https://doi.org/10.1126/science.289.5480.751.

(12) Dutz, S. Are Magnetic Multicore Nanoparticles Promising Candidates for Biomedical Applications? *IEEE Trans. Magn.* **2016**, *52* (9), 1–3. https://doi.org/10.1109/TMAG.2016.2570745.

(13) Jefremovas, E. M.; Gandarias, L.; Rodrigo, I.; Marcano, L.; Gruttner, C.; Garcia, J. A.; Garayo, E.; Orue, I.; Garcia-Prieto, A.; Muela, A.; Fernandez-Gubieda, M. L.; Alonso, J.; Barquin, L. F. Nanoflowers Versus Magnetosomes: Comparison Between Two Promising Candidates for Magnetic Hyperthermia Therapy. *IEEE Access* **2021**, *9*, 99552–99561. https://doi.org/10.1109/ACCESS.2021.3096740.

(14) Kostopoulou, A.; Lappas, A. Colloidal Magnetic Nanocrystal Clusters: Variable Length-Scale Interaction Mechanisms, Synergetic Functionalities and Technological Advantages. *Nanotechnol. Rev.* **2015**, *4* (6). https://doi.org/10.1515/ntrev-2014-0034.

(15) Xiao, Z.; Zhang, L.; Colvin, V. L.; Zhang, Q.; Bao, G. Synthesis and Application of Magnetic Nanocrystal Clusters. *Ind. Eng. Chem. Res.* **2022**, *61* (22), 7613–7625. https://doi.org/10.1021/acs.iecr.1c04879.

(16) Hugounenq, P.; Levy, M.; Alloyeau, D.; Lartigue, L.; Dubois, E.; Cabuil, V.; Ricolleau, C.; Roux, S.; Wilhelm, C.; Gazeau, F.; Bazzi, R. Iron Oxide Monocrystalline Nanoflowers for Highly Efficient Magnetic Hyperthermia. *J. Phys. Chem. C* **2012**, *116* (29), 15702–15712. https://doi.org/10.1021/jp3025478.
(17) Maity, D.; Kale, S. N.; Kaul-Ghanekar, R.; Xue, J.-M.; Ding, J. Studies of Magnetite Nanoparticles Synthesized by Thermal Decomposition of Iron (III) Acetylacetonate in Tri(Ethylene Glycol). *J. Magn. Magn. Mater.* **2009**, *321* (19), 3093–3098. https://doi.org/10.1016/j.jmmm.2009.05.020.
(18) Bunge, A.; Porav, A. S.; Borodi, G.; Radu, T.; Pîrnău, A.; Berghian-Grosan, C.; Turcu, R. Correlation between Synthesis Parameters and Properties of Magnetite Clusters Prepared by Solvothermal Polyol Method. *J. Mater. Sci.* **2019**, *54* (4), 2853–2875. https://doi.org/10.1007/s10853-018-3030-9.
(19) Sakellari, D.; Brintakis, K.; Kostopoulou, A.; Myrovali, E.; Simeonidis, K.; Lappas, A.; Angelakeris, M. Ferrimagnetic Nanocrystal Assemblies as Versatile Magnetic Particle Hyperthermia Mediators. *Mater. Sci. Eng. C* **2016**, *58*, 187–193. https://doi.org/10.1016/j.msec.2015.08.023.
(20) Wei, X.; Jing, L.; Liu, C.; Hou, Y.; Jiao, M.; Gao, M. Molecular Mechanisms for Delicately Tuning the Morphology and Properties of Fe_3O_4 Nanoparticle Clusters. *CrystEngComm* **2018**, *20* (17), 2421–2429. https://doi.org/10.1039/C8CE00056E.
(21) Mandić, L.; Sadžak, A.; Erceg, I.; Baranović, G.; Šegota, S. The Fine-Tuned Release of Antioxidant from Superparamagnetic Nanocarriers under the Combination of Stationary and Alternating Magnetic Fields. *Antioxidants* **2021**, *10* (8), 1212. https://doi.org/10.3390/antiox10081212.
(22) Hu, F.; MacRenaris, K. W.; Waters, E. A.; Schultz-Sikma, E. A.; Eckermann, A. L.; Meade, T. J. Highly Dispersible, Superparamagnetic Magnetite Nanoflowers for Magnetic Resonance Imaging. *Chem. Commun.* **2010**, *46* (1), 73–75. https://doi.org/10.1039/B916562B.
(23) Xuan, S.; Wang, Y.-X. J.; Yu, J. C.; Cham-Fai Leung, K. Tuning the Grain Size and Particle Size of Superparamagnetic Fe_3O_4 Microparticles. *Chem. Mater.* **2009**, *21* (21), 5079–5087. https://doi.org/10.1021/cm901618m.
(24) Hachani, R.; Lowdell, M.; Birchall, M.; Hervault, A.; Mertz, D.; Begin-Colin, S.; Thanh, N. T. K. Polyol Synthesis, Functionalisation, and Biocompatibility Studies of Superparamagnetic Iron Oxide Nanoparticles as Potential MRI Contrast Agents. *Nanoscale* **2016**, *8* (6), 3278–3287. https://doi.org/10.1039/C5NR03867G.
(25) Gaudisson, T.; Sayed-Hassan, R.; Yaacoub, N.; Franceschin, G.; Nowak, S.; Grenèche, J.-M.; Menguy, N.; Sainctavit, P.; Ammar, S. On the Exact Crystal Structure of Exchange-Biased Fe3O4–CoO Nanoaggregates Produced by Seed-Mediated Growth in Polyol. *CrystEngComm* **2016**, *18* (21), 3799–3807. https://doi.org/10.1039/C6CE00700G.
(26) Spizzo, F.; Sgarbossa, P.; Sieni, E.; Semenzato, A.; Dughiero, F.; Forzan, M.; Bertani, R.; Del Bianco, L. Synthesis of Ferrofluids Made of Iron Oxide Nanoflowers: Interplay between Carrier Fluid and Magnetic Properties. *Nanomaterials* **2017**, *7* (11), 373. https://doi.org/10.3390/nano7110373.
(27) Zhang, B.; Tu, Z.; Zhao, F.; Wang, J. Superparamagnetic Iron Oxide Nanoparticles Prepared by Using an Improved Polyol Method. *Appl. Surf. Sci.* **2013**, *266*, 375–379. https://doi.org/10.1016/j.apsusc.2012.12.032.
(28) Nikitin, A. A.; Shchetinin, I. V.; Tabachkova, N. Yu.; Soldatov, M. A.; Soldatov, A. V.; Sviridenkova, N. V.; Beloglazkina, E. K.; Savchenko, A. G.; Fedorova, N. D.; Abakumov, M. A.; Majouga, A. G. Synthesis of Iron Oxide Nanoclusters by Thermal Decomposition. *Langmuir* **2018**, *34* (15), 4640–4650. https://doi.org/10.1021/acs.langmuir.8b00753.
(29) Kratz, H.; Taupitz, M.; Schellenberger, A. A. de; Kosch, O.; Eberbeck, D.; Wagner, S.; Trahms, L.; Hamm, B.; Schnorr, J. Novel Magnetic Multicore Nanoparticles Designed for MPI and Other Biomedical Applications: From Synthesis to First in Vivo Studies. *PLOS ONE* **2018**, *13* (1), e0190214. https://doi.org/10.1371/journal.pone.0190214.
(30) Zoppellaro, G.; Kolokithas-Ntoukas, A.; Polakova, K.; Tucek, J.; Zboril, R.; Loudos, G.; Fragogeorgi, E.; Diwoky, C.; Tomankova, K.; Avgoustakis, K.; Kouzoudis, D.; Bakandritsos, A. Theranostics of Epitaxially

Condensed Colloidal Nanocrystal Clusters, through a Soft Biomineralization Route. *Chem. Mater.* **2014**, *26* (6), 2062–2074. https://doi.org/10.1021/cm404053v.

(31) Hemery, G.; Keyes, A. C.; Garaio, E.; Rodrigo, I.; Garcia, J. A.; Plazaola, F.; Garanger, E.; Sandre, O. Tuning Sizes, Morphologies, and Magnetic Properties of Monocore Versus Multicore Iron Oxide Nanoparticles through the Controlled Addition of Water in the Polyol Synthesis. *Inorg. Chem.* **2017**, *56* (14), 8232–8243. https://doi.org/10.1021/acs.inorgchem.7b00956.

(32) Gavilán, H.; Kowalski, A.; Heinke, D.; Sugunan, A.; Sommertune, J.; Varón, M.; Bogart, L. K.; Posth, O.; Zeng, L.; González-Alonso, D.; Balceris, C.; Fock, J.; Wetterskog, E.; Frandsen, C.; Gehrke, N.; Grüttner, C.; Fornara, A.; Ludwig, F.; Veintemillas-Verdaguer, S.; Johansson, C.; Morales, M. P. Colloidal Flower-Shaped Iron Oxide Nanoparticles: Synthesis Strategies and Coatings. *Part. Part. Syst. Charact.* **2017**, *34* (7), 1700094. https://doi.org/10.1002/ppsc.201700094.

(33) Gavilán, H.; Simeonidis, K.; Myrovali, E.; Mazarío, E.; Chubykalo-Fesenko, O.; Chantrell, R.; Balcells, L.; Angelakeris, M.; P. Morales, M.; Serantes, D. How Size, Shape and Assembly of Magnetic Nanoparticles Give Rise to Different Hyperthermia Scenarios. *Nanoscale* **2021**, *13* (37), 15631–15646. https://doi.org/10.1039/D1NR03484G.

(34) Hergt, R.; Dutz, S.; Röder, M. Effects of Size Distribution on Hysteresis Losses of Magnetic Nanoparticles for Hyperthermia. *J. Phys. Condens. Matter* **2008**, *20* (38), 385214. https://doi.org/10.1088/0953-8984/20/38/385214.

(35) Lee, J.-H.; Jang, J.; Choi, J.; Moon, S. H.; Noh, S.; Kim, J.; Kim, J.-G.; Kim, I.-S.; Park, K. I.; Cheon, J. Exchange-Coupled Magnetic Nanoparticles for Efficient Heat Induction. *Nat. Nanotechnol.* **2011**, *6* (7), 418–422. https://doi.org/10.1038/nnano.2011.95.

(36) Rosensweig, R. E. Heating Magnetic Fluid with Alternating Magnetic Field. *J. Magn. Magn. Mater.* **2002**, *252*, 370–374. https://doi.org/10.1016/S0304-8853(02)00706-0.

(37) Carrey, J.; Mehdaoui, B.; Respaud, M. Simple Models for Dynamic Hysteresis Loop Calculations of Magnetic Single-Domain Nanoparticles: Application to Magnetic Hyperthermia Optimization. *J. Appl. Phys.* **2011**, *109* (8), 083921. https://doi.org/10.1063/1.3551582.

(38) Levy, M.; Quarta, A.; Espinosa, A.; Figuerola, A.; Wilhelm, C.; García-Hernández, M.; Genovese, A.; Falqui, A.; Alloyeau, D.; Buonsanti, R.; Cozzoli, P. D.; García, M. A.; Gazeau, F.; Pellegrino, T. Correlating Magneto-Structural Properties to Hyperthermia Performance of Highly Monodisperse Iron Oxide Nanoparticles Prepared by a Seeded-Growth Route. *Chem. Mater.* **2011**, *23* (18), 4170–4180. https://doi.org/10.1021/cm201078f.

(39) Fortin, J.-P.; Wilhelm, C.; Servais, J.; Ménager, C.; Bacri, J.-C.; Gazeau, F. Size-Sorted Anionic Iron Oxide Nanomagnets as Colloidal Mediators for Magnetic Hyperthermia. *J. Am. Chem. Soc.* **2007**, *129* (9), 2628–2635. https://doi.org/10.1021/ja067457e.

(40) Mehdaoui, B.; Meffre, A.; Carrey, J.; Lachaize, S.; Lacroix, L.-M.; Gougeon, M.; Chaudret, B.; Respaud, M. Optimal Size of Nanoparticles for Magnetic Hyperthermia: A Combined Theoretical and Experimental Study. *Adv. Funct. Mater.* **2011**, *21* (23), 4573–4581. https://doi.org/10.1002/adfm.201101243.

(41) Lévy, M.; Wilhelm, C.; Siaugue, J.-M.; Horner, O.; Bacri, J.-C.; Gazeau, F. Magnetically Induced Hyperthermia: Size-Dependent Heating Power of γ-Fe(2)O(3) Nanoparticles. *J. Phys. Condens. Matter Inst. Phys. J.* **2008**, *20* (20), 204133. https://doi.org/10.1088/0953-8984/20/20/204133.

(42) Martinez-Boubeta, C.; Simeonidis, K.; Makridis, A.; Angelakeris, M.; Iglesias, O.; Guardia, P.; Cabot, A.; Yedra, L.; Estradé, S.; Peiró, F.; Saghi, Z.; Midgley, P. A.; Conde-Leborán, I.; Serantes, D.; Baldomir, D. Learning from Nature to Improve the Heat Generation of Iron-Oxide Nanoparticles for Magnetic Hyperthermia Applications. *Sci. Rep.* **2013**, *3* (1), 1652. https://doi.org/10.1038/srep01652.

(43) Guardia, P.; Corato, R. D.; Lartigue, L.; Wilhelm, C.; Espinosa, A.; Garcia-Hernandez, M.; Gazeau, F.; Manna, L.; Pellegrino, T. Water-Soluble Iron Oxide Nanocubes with High Values of Specific Absorption Rate for Cancer Cell Hyperthermia Treatment. **2012**, *6* (4), 12.

(44) Blanco-Andujar, C.; Ortega, D.; Southern, P.; Pankhurst, Q. A.; Thanh, N. T. K. High Performance Multi-Core Iron Oxide Nanoparticles for Magnetic Hyperthermia: Microwave Synthesis, and the Role of Core-to-Core Interactions. *Nanoscale* **2015**, *7* (5), 1768–1775. https://doi.org/10.1039/C4NR06239F.
(45) Storozhuk, L.; Besenhard, M. O.; Mourdikoudis, S.; LaGrow, A. P.; Lees, M. R.; Tung, L. D.; Gavriilidis, A.; Thanh, N. T. K. Stable Iron Oxide Nanoflowers with Exceptional Magnetic Heating Efficiency: Simple and Fast Polyol Synthesis. *ACS Appl. Mater. Interfaces* **2021**, *13* (38), 45870–45880. https://doi.org/10.1021/acsami.1c12323.
(46) Lak, A.; Disch, S.; Bender, P. Embracing Defects and Disorder in Magnetic Nanoparticles. *Adv. Sci.* **2021**, *8* (7), 2002682. https://doi.org/10.1002/advs.202002682.
(47) Bertuit, E.; Benassai, E.; Mériguet, G.; Greneche, J.-M.; Baptiste, B.; Neveu, S.; Wilhelm, C.; Abou-Hassan, A. Structure–Property–Function Relationships of Iron Oxide Multicore Nanoflowers in Magnetic Hyperthermia and Photothermia. *ACS Nano* **2022**, *16* (1), 271–284. https://doi.org/10.1021/acsnano.1c06212.
(48) Krishnan, K. M. Biomedical Nanomagnetics: A Spin Through Possibilities in Imaging, Diagnostics, and Therapy. *IEEE Trans. Magn.* **2010**, *46* (7), 2523–2558. https://doi.org/10.1109/TMAG.2010.2046907.
(49) Pankhurst, Q. A.; Thanh, N. T. K.; Jones, S. K.; Dobson, J. Progress in Applications of Magnetic Nanoparticles in Biomedicine. *J. Phys. Appl. Phys.* **2009**, *42* (22), 224001. https://doi.org/10.1088/0022-3727/42/22/224001.
(50) Garaio, E.; Collantes, J. M.; Plazaola, F.; Garcia, J. A.; Castellanos-Rubio, I. A Multifrequency Eletromagnetic Applicator with an Integrated AC Magnetometer for Magnetic Hyperthermia Experiments. *Meas. Sci. Technol.* **2014**, *25* (11), 115702. https://doi.org/10.1088/0957-0233/25/11/115702.
(51) Garaio, E.; Collantes, J. M.; Garcia, J. A.; Plazaola, F.; Mornet, S.; Couillaud, F.; Sandre, O. A Wide-Frequency Range AC Magnetometer to Measure the Specific Absorption Rate in Nanoparticles for Magnetic Hyperthermia. *J. Magn. Magn. Mater.* **2014**, *368*, 432–437. https://doi.org/10.1016/j.jmmm.2013.11.021.
(52) Guibert, C.; Fresnais, J.; Peyre, V.; Dupuis, V. Magnetic Fluid Hyperthermia Probed by Both Calorimetric and Dynamic Hysteresis Measurements. *J. Magn. Magn. Mater.* **2017**, *421*, 384–392. https://doi.org/10.1016/j.jmmm.2016.08.015.
(53) Wells, J.; Kosch, O.; Wiekhorst, F. Multi-Frequency Hyperthermia Characterisation via Calorimetry and AC Magnetometry Measurements. *J. Magn. Magn. Mater.* **2022**, *563*, 169992. https://doi.org/10.1016/j.jmmm.2022.169992.
(54) Engelmann, U. M.; Shasha, C.; Slabu, I. Magnetic Nanoparticle Relaxation in Biomedical Application. In *Magnetic Nanoparticles in Human Health and Medicine*; John Wiley & Sons, Ltd, 2021; pp 327–354. https://doi.org/10.1002/9781119754725.ch15.
(55) Engelmann, U. M.; Shasha, C.; Teeman, E.; Slabu, I.; Krishnan, K. M. Predicting Size-Dependent Heating Efficiency of Magnetic Nanoparticles from Experiment and Stochastic Néel-Brown Langevin Simulation. *J. Magn. Magn. Mater.* **2019**, *471*, 450–456. https://doi.org/10.1016/j.jmmm.2018.09.041.
(56) Tourinho, F. A.; Franck, R.; Massart, R. Aqueous Ferrofluids Based on Manganese and Cobalt Ferrites. *J. Mater. Sci.* **1990**, *25* (7), 3249–3254. https://doi.org/10.1007/BF00587682.
(57) Rad, A. M.; Janic, B.; Iskander, A.; Soltanian-Zadeh, H.; Arbab, A. S. Measurement of Quantity of Iron in Magnetically Labeled Cells: Comparison among Different UV/VIS Spectrometric Methods. *BioTechniques* **2007**, *43* (5), 627–636. https://doi.org/10.2144/000112599.
(58) de la Calle, I.; Menta, M.; Klein, M.; Maxit, B.; Séby, F. Towards Routine Analysis of TiO 2 (Nano-)Particle Size in Consumer Products: Evaluation of Potential Techniques. *Spectrochim. Acta Part B At. Spectrosc.* **2018**, *147*, 28–42. https://doi.org/10.1016/j.sab.2018.05.012.
(59) *Laser Light Scattering*; CRC Press, 2018; pp 177–248. https://doi.org/10.1201/9781351076814-5.

(60) Bertuit, E.; Menguy, N.; Wilhelm, C.; Rollet, A.-L.; Abou-Hassan, A. Angular Orientation between the Cores of Iron Oxide Nanoclusters Controls Their Magneto–Optical Properties and Magnetic Heating Functions. *Commun. Chem.* **2022**, *5* (1), 1–10. https://doi.org/10.1038/s42004-022-00787-0.

(61) Gallo-Cordova, Á.; Espinosa, A.; Serrano, A.; Gutiérrez, L.; Menéndez, N.; del Puerto Morales, M.; Mazarío, E. New Insights into the Structural Analysis of Maghemite and (MFe_2O_4, M = Co, Zn) Ferrite Nanoparticles Synthesized by a Microwave-Assisted Polyol Process. *Mater. Chem. Front.* **2020**, *4* (10), 3063–3073. https://doi.org/10.1039/D0QM00460J.

(62) Thanh, N. T. K.; Maclean, N.; Mahiddine, S. Mechanisms of Nucleation and Growth of Nanoparticles in Solution. *Chem. Rev.* **2014**, *114* (15), 7610–7630. https://doi.org/10.1021/cr400544s.

(63) Lartigue, L.; Hugounenq, P.; Alloyeau, D.; Clarke, S. P.; Lévy, M.; Bacri, J.-C.; Bazzi, R.; Brougham, D. F.; Wilhelm, C.; Gazeau, F. Cooperative Organization in Iron Oxide Multi-Core Nanoparticles Potentiates Their Efficiency as Heating Mediators and MRI Contrast Agents. *ACS Nano* **2012**, *6* (12), 10935–10949. https://doi.org/10.1021/nn304477s.

(64) Demortière, A.; Panissod, P.; Pichon, B. P.; Pourroy, G.; Guillon, D.; Donnio, B.; Bégin-Colin, S. Size-Dependent Properties of Magnetic Iron Oxide Nanocrystals. *Nanoscale* **2011**, *3* (1), 225–232. https://doi.org/10.1039/C0NR00521E.

(65) Park, J.; Lee, E.; Hwang, N.-M.; Kang, M.; Kim, S. C.; Hwang, Y.; Park, J.-G.; Noh, H.-J.; Kim, J.-Y.; Park, J.-H.; Hyeon, T. One-Nanometer-Scale Size-Controlled Synthesis of Monodisperse Magnetic Iron Oxide Nanoparticles. *Angew. Chem. Int. Ed.* **2005**, *44* (19), 2872–2877. https://doi.org/10.1002/anie.200461665.

(66) Tang, J.; Myers, M.; Bosnick, K. A.; Brus, L. E. Magnetite Fe3O4 Nanocrystals: Spectroscopic Observation of Aqueous Oxidation Kinetics. *J. Phys. Chem. B* **2003**, *107* (30), 7501–7506. https://doi.org/10.1021/jp027048e.

(67) Judith Vijaya, J.; Sekaran, G.; Bououdina, M. Effect of Cu2+ Doping on Structural, Morphological, Optical and Magnetic Properties of MnFe2O4 Particles/Sheets/Flakes-like Nanostructures. *Ceram. Int.* **2015**, *41* (1), 15–26. https://doi.org/10.1016/j.ceramint.2013.10.145.

(68) Maibam, B.; Baruah, S.; Kumar, S. Photoluminescence and Intrinsic Ferromagnetism of Fe Doped Zinc Oxide. *SN Appl. Sci.* **2020**, *2* (10), 1712. https://doi.org/10.1007/s42452-020-03519-y.

(69) Shaw, S. K.; Kailashiya, J.; Gangwar, A.; Alla, S. K.; Gupta, S. K.; Prajapat, C. L.; Meena, S. S.; Dash, D.; Maiti, P.; Prasad, N. K. γ-Fe2O3 Nanoflowers as Efficient Magnetic Hyperthermia and Photothermal Agent. *Appl. Surf. Sci.* **2021**, *560*, 150025. https://doi.org/10.1016/j.apsusc.2021.150025.

(70) Sadat, S. M. A.; Jahan, S. T.; Haddadi, A. Effects of Size and Surface Charge of Polymeric Nanoparticles on <I>in Vitro</I> and <I>in Vivo</I> Applications. *J. Biomater. Nanobiotechnology* **2016**, *07* (02), 91–108. https://doi.org/10.4236/jbnb.2016.72011.

(71) Shingte, S. D.; Phakatkar, A. H.; McKiernan, E.; Nigoghossian, K.; Ferguson, S.; Shahbazian-Yassar, R.; Brougham, D. F. Correlating Magnetic Hyperthermia and Magnetic Resonance Imaging Contrast Performance of Cubic Iron Oxide Nanoparticles with Crystal Structural Integrity. *Chem. Mater.* **2022**, acs.chemmater.2c00708. https://doi.org/10.1021/acs.chemmater.2c00708.

(72) Garaio, E.; Sandre, O.; Collantes, J.-M.; Garcia, J. A.; Mornet, S.; Plazaola, F. Specific Absorption Rate Dependence on Temperature in Magnetic Field Hyperthermia Measured by Dynamic Hysteresis Losses (Ac Magnetometry). *Nanotechnology* **2015**, *26* (1), 015704. https://doi.org/10.1088/0957-4484/26/1/015704.

(73) Engelmann, U. M.; Fitter, J. L.; Baumann, M. Assessing Magnetic Fluid Hyperthermia : Magnetic Relaxation Simulation, Modeling of Nanoparticle Uptake inside Pancreatic Tumor Cells and in Vitro Efficacy, Infinite Science Publishing, 2019. https://publications.rwth-aachen.de/record/760388 (accessed 2022-08-11).

(74) Micha, J. S.; Dieny, B.; Régnard, J. R.; Jacquot, J. F.; Sort, J. Estimation of the Co Nanoparticles Size by Magnetic Measurements in Co/SiO2 Discontinuous Multilayers. *J. Magn. Magn. Mater.* **2004**, *272–276*, E967–E968. https://doi.org/10.1016/j.jmmm.2003.12.268.

(75) Bruvera, I. J.; Mendoza Zélis, P.; Pilar Calatayud, M.; Goya, G. F.; Sánchez, F. H. Determination of the Blocking Temperature of Magnetic Nanoparticles: The Good, the Bad, and the Ugly. *J. Appl. Phys.* **2015**, *118* (18), 184304. https://doi.org/10.1063/1.4935484.

(76) Cotin, G.; Blanco-Andujar, C.; Perton, F.; Asín, L.; de la Fuente, J. M.; Reichardt, W.; Schaffner, D.; Ngyen, D.-V.; Mertz, D.; Kiefer, C.; Meyer, F.; Spassov, S.; Ersen, O.; Chatzidakis, M.; Botton, G. A.; Hénoumont, C.; Laurent, S.; Greneche, J.-M.; Teran, F. J.; Ortega, D.; Felder-Flesch, D.; Begin-Colin, S. Unveiling the Role of Surface, Size, Shape and Defects of Iron Oxide Nanoparticles for Theranostic Applications. *Nanoscale* **2021**, *13* (34), 14552–14571. https://doi.org/10.1039/D1NR03335B.

(77) Wu, K.; Su, D.; Saha, R.; Liu, J.; Wang, J.-P. Investigating the Effect of Magnetic Dipole–Dipole Interaction on Magnetic Particle Spectroscopy: Implications for Magnetic Nanoparticle-Based Bioassays and Magnetic Particle Imaging. *J. Phys. Appl. Phys.* **2019**, *52* (33), 335002. https://doi.org/10.1088/1361-6463/ab2580.

(78) Mørup, S.; Bo Madsen, M.; Franck, J.; Villadsen, J.; Koch, C. J. W. A New Interpretation of Mössbauer Spectra of Microcrystalline Goethite: "Super-Ferromagnetism" or "Super-Spin-Glass" Behaviour? *J. Magn. Magn. Mater.* **1983**, *40* (1–2), 163–174. https://doi.org/10.1016/0304-8853(83)90024-0.

(79) Bedanta, S.; Kleemann, W. Supermagnetism. *J. Phys. Appl. Phys.* **2009**, *42* (1), 013001. https://doi.org/10.1088/0022-3727/42/1/013001.

(80) Bender, P.; Fock, J.; Frandsen, C.; Hansen, M. F.; Balceris, C.; Ludwig, F.; Posth, O.; Wetterskog, E.; Bogart, L. K.; Southern, P.; Szczerba, W.; Zeng, L.; Witte, K.; Grüttner, C.; Westphal, F.; Honecker, D.; González-Alonso, D.; Fernández Barquín, L.; Johansson, C. Relating Magnetic Properties and High Hyperthermia Performance of Iron Oxide Nanoflowers. *J. Phys. Chem. C* **2018**, *122* (5), 3068–3077. https://doi.org/10.1021/acs.jpcc.7b11255.

(81) Pisane, K. Effects of Size and Size Distribution on the Magnetic Properties of Maghemite Nanoparticles and Iron-Platinum Core-Shell Nanoparticles. PhD, West Virginia University Libraries, 2015. https://doi.org/10.33915/etd.6423.

(82) Komorida, Y.; Mito, M.; Deguchi, H.; Takagi, S.; Millán, A.; Silva, N. J. O.; Palacio, F. Surface and Core Magnetic Anisotropy in Maghemite Nanoparticles Determined by Pressure Experiments. *Appl. Phys. Lett.* **2009**, *94* (20), 202503. https://doi.org/10.1063/1.3131782.

(83) Dormann, J. L.; D'Orazio, F.; Lucari, F.; Tronc, E.; Prene, P.; Jolivet, J. P.; Fiorani, D.; Cherkaoui, R.; Nogues, M. Thermal Variation of the Relaxation Time of the Magnetic Moment of □-Fe2O3 Nanoparticles with Interparticle Interactions of Various Strengths. 7.

(84) Usov, N. A. Low Frequency Hysteresis Loops of Superparamagnetic Nanoparticles with Uniaxial Anisotropy. *J. Appl. Phys.* **2010**, *107* (12), 123909. https://doi.org/10.1063/1.3445879.

(85) Marciello, M.; Connord, V.; Veintemillas-Verdaguer, S.; Vergés, M. A.; Carrey, J.; Respaud, M.; Serna, C. J.; Morales, M. P. Large Scale Production of Biocompatible Magnetite Nanocrystals with High Saturation Magnetization Values through Green Aqueous Synthesis. *J. Mater. Chem. B* **2013**, *1* (43), 5995. https://doi.org/10.1039/c3tb20949k.

(86) Bertuit, E.; Neveu, S.; Abou-Hassan, A. High Temperature Continuous Flow Syntheses of Iron Oxide Nanoflowers Using the Polyol Route in a Multi-Parametric Millifluidic Device. *Nanomaterials* **2021**, *12* (1), 119. https://doi.org/10.3390/nano12010119.

(87) Ruta, S.; Chantrell, R.; Hovorka, O. Unified Model of Hyperthermia via Hysteresis Heating in Systems of Interacting Magnetic Nanoparticles. *Sci. Rep.* **2015**, *5* (1), 9090. https://doi.org/10.1038/srep09090.

(88) Atkinson, W. J.; Brezovich, I. A.; Chakraborty, D. P. Usable Frequencies in Hyperthermia with Thermal Seeds. *IEEE Trans. Biomed. Eng.* **1984**, *BME-31* (1), 70–75. https://doi.org/10.1109/TBME.1984.325372.